

MASTER'S THESIS APPLIED PHYSICS

The role of surface plasmons in metal-enhanced chemiluminescence

Jesse Mak

February 7, 2014



GRADUATION COMMITTEE

Prof. Dr. Jennifer L. Herek^a

Prof. Dr. Ir. Alexander Brinkman^b

Dr. Christian Blum^c

Dr. Jord C. Prangsma^{a,c}

^a Optical Sciences group, ^b Quantum Transport in Matter group, ^c Nanobiophysics group

Optical Sciences group and Nanobiophysics group
Faculty of Science and Technology
University of Twente

AUTHOR

Jesse Mak

jesse.mak@gmail.com

GRADUATION COMMITTEE

Prof. Dr. Jennifer L. Herek^a

Prof. Dr. Ir. Alexander Brinkman^b

Dr. Christian Blum^c

Dr. Jord C. Prangsma^{a,c}

^a Optical Sciences group, ^b Quantum Transport in Matter group, ^c Nanobiophysics group

Optical Sciences group and Nanobiophysics group

Faculty of Science and Technology

University of Twente

Contents

Acknowledgements	1
Abstract	2
1 Introduction	3
2 Chemiluminescence	6
2.1 Mechanism of chemiluminescence	6
2.2 Efficiency of chemiluminescence	7
3 Optical antennas	9
3.1 The complex dielectric function of metals	10
3.2 Plasmonic resonances in quasi-static structures	11
3.3 Plasmonic resonances in elongated structures	13
4 Luminescence near optical antennas	15
4.1 Radiative and non-radiative decay near an antenna	15
4.2 Model for enhancement	16
4.3 Plasmon-enhanced chemiluminescence	18
5 Experimental aspects	19
5.1 Antenna sample	19
5.1.1 Design and fabrication	19
5.1.2 Scanning electron microscope inspection	21
5.1.3 Sample cleaning	21
5.2 Dark field characterization setup	22
5.2.1 Experimental setup	22
5.2.2 Typical dark field spectrum	22
5.3 Fluorescence microscope	23
5.3.1 Experimental setup	23
5.3.2 Typical gold luminescence spectrum	24
5.3.3 Typical fluorescence time trace	26
6 Results and discussion	27
6.1 Dark field scattering spectra	27
6.2 Gold luminescence spectra	29
6.3 Resonances compared to theory	31

6.4	Lucigenin fluorescence and chemiluminescence	33
6.5	Methylene blue fluorescence	36
6.5.1	Measured time traces	36
6.5.2	Analysis using photon count histograms	38
6.5.3	Comparison of different-sized antennas	39
6.5.4	Control experiment using water	40
7	Conclusion and outlook	43
	References	45
A	Details of the experiments with the fluorescence microscope	49

Acknowledgements

First of all, I would like to thank Jord, my daily supervisor, for his devotion to the project, his insightful explanations, and original ideas. It was a pleasure to work with you Jord. I would also like to thank Dirk Jan, who helped with experiments and provided valuable feedback on the project.

Furthermore, my thanks go out to Stefan for synthesizing gold flakes, to Frans for his excellent work with the focused ion beam, and to Ron Gill for providing me with an interesting fluorescent dye. I also thank Tom and Simon for their motivating and calming support. I particularly thank Simon for his advice on presenting my work.

I thank Jeroen for additional technical support and Karen and Carin for administrative support. In fact, I am grateful to everyone in the Optical Sciences and Nanobiophysics groups for their contributions to the project and for the great social atmosphere.

I would like to thank Jennifer Herek for motivating and supporting me throughout the MSc programme. I especially thank her for arranging an amazing internship in Boulder. Next, I would like to thank my friends for the great time in Enschede. Special thanks to Sean, Luuk, Murat, and Roza, to student fraternity Πίθηχος άμάρτανοι, and to student house Da Bunch. Finally, I am very grateful to Franziska and my family for their support.

Jesse Mak

February 2014

Abstract

Chemiluminescence is used in many analysis methods as a sensitive reporter of the presence of biological materials. In a chemiluminescent process, a chemical reaction involving the substance of interest leads to a reaction product in the excited state. This excited state can decay by the emission of photons. However, the quantum efficiency of this process is often low due to a multitude of non-radiative decay paths. Enhancing the radiative decay of the excited state is therefore of wide interest. Several studies have been performed to investigate the use of plasmons for this [1] however, none of these studies made use of plasmonic systems with well-characterized resonances.

We study lucigenin chemiluminescence and methylene blue fluorescence near different-sized optical antennas. The plasmon resonances were characterized using 1) dark-field scattering spectroscopy and 2) spectroscopy of the intrinsic luminescence of the antenna material (gold). We observe an approximately linear relation between the resonance wavelength and antenna length, which is in good agreement with a Fabry-Perot resonator model for cylindrical antennas [2].

Lucigenin chemiluminescence has two major components that emit light: 1) N-methyl acridone, and 2) the lucigenin itself, excited by N-methyl acridone through Förster resonance energy transfer. We first study the emission of the second component, with excitation by light. Following this, we study the complete chemiluminescent system. We show that the antennas in fact *darken* the emission, and explore several explanations.

The final part of the thesis presents a controlled study on the distance dependent enhancement of a fluorophore near an antenna. We observe fluorescence time traces with strong peaks whenever an emitter is in a favorable location with respect to the antenna, where enhancement occurs. Most intensity enhancement is observed for a 70x110 nm antenna, with an enhancement factor of ~4.

We pioneer the use of photon count histograms as a tool to analyze the fluorescence peaks. We show that the histograms form a strong signature of enhanced emission near an optical antenna. We anticipate that this method could be generalized to provide subdiffraction-limited information on spatially-varying enhancement near a nanostructure.

1 Introduction

Sensitive detection of molecules is of central importance for a number of fields, such as pharmacology, bioscience, and environmental science [3]. An established method to detect molecules is to involve them in chemical reactions that produce light. This type of light emission is called *chemiluminescence*. It is routinely used as a reporter for molecules in clinical tests on, e.g., fertility, anemia, cancer, or infectious diseases [4]. In bioscience, it is used to mark the location of biological macromolecules (DNA, RNA, proteins) that have been sorted using membrane filters [4]. Other applications include the detection of environmental pollutants [3] and the detection of blood in crime scene investigation [5].

Chemiluminescence-based techniques have advantages over other detection techniques. In contrast to fluorescence-based detection, no external light source is required. Therefore, problems such as light scattering, source fluctuations, and high backgrounds due to unselective excitation are absent [6]. Furthermore, chemiluminescence reagents are considered to be less hazardous than alternative techniques using radioactive isotopes for tracing chemicals [6].

In a chemiluminescent process a chemical reaction involving the substance of interest leads to a reaction product in an electronically excited state (see Fig. 1.1). This excited state can decay by the emission of photons. However, the efficiency of this process is often low due to a multitude of non-radiative decay pathways. Enhancing the radiative decay of the excited state is therefore of wide interest.

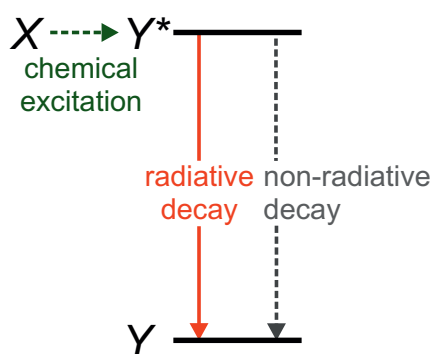


Figure 1.1: Simplified energy level diagram for chemiluminescence. A chemical reaction involving X leads to a reaction product in the excited state (Y^*). The excited state can make a transition to the ground state (Y) with the emission of a photon (radiative decay), but it can also return to the ground state by a radiationless process (non-radiative decay).

It is well-known that the radiative decay rate of a quantum emitter can be increased by optimizing the nanoscale environment by, e.g., reflecting interfaces, photonic crystals, or plas-

monic nano-antennas [7]. Near an optical antenna, the radiative rate can increase because there are more pathways that lead to the radiation of a photon to the far-field. This is one of the reasons why fluorescence shows an enhanced intensity near metal plasmonic nanostructures [8, 9].

Several groups also report an enhanced *chemiluminescence* intensity near metal plasmonic structures [1, 10, 11]. An example of these findings is shown in Fig. 1.2 [1]. We note that none of the studies made use of plasmonic systems with well-characterized resonances. As many chemiluminescent reactions require a catalyst [6], the metal may also catalyze (*i.e.* speed up) the reaction. In that case, the photons would be emitted within a shorter time-window, leading to a higher chemiluminescence intensity. Therefore, it is debatable whether there is enough evidence to ascribe the enhancement to plasmons.

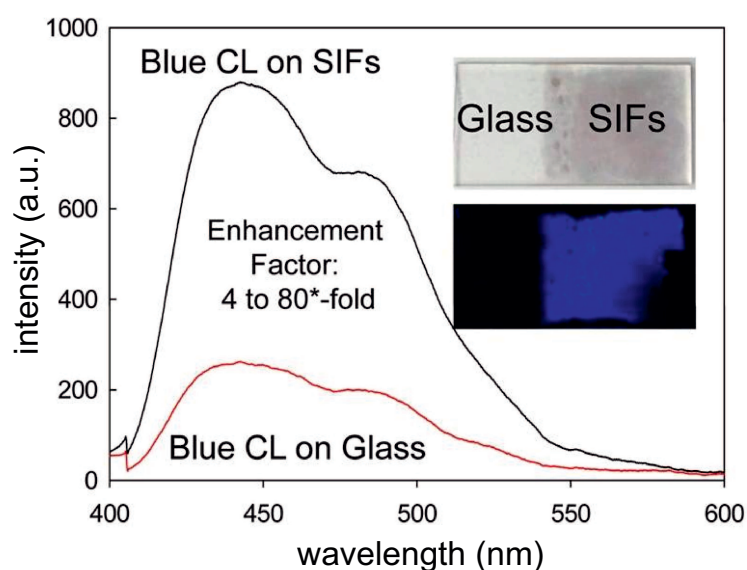


Figure 1.2: Enhanced chemiluminescence (CL) on silver island films (SIFs). The graph shows chemiluminescence spectra on silver island films (black curve) and on glass (red curve). The insets show photographs of a glass microscope slide with silver island films (top) and the chemiluminescent mixture placed in between two slides (bottom). From Aslan and Geddes [1].

The aim of this research is to find evidence whether enhanced chemiluminescence can be ascribed to a plasmonic effect, a catalytic effect, or a combination of these. In contrast to earlier work, we aim to study chemiluminescence near a plasmonic system where the geometry and optical properties are well characterized. For this reason, we designed an array gold antennas with well-defined lengths (Fig. 1.3). Such antennas have resonant plasmon modes at different wavelengths [2], and will only enhance emission of light with a similar wavelength. By comparing the chemiluminescence intensity near each antenna, we hope to find out whether enhanced chemiluminescence is a resonant plasmonic effect.

Following design and fabrication of the antennas, we characterized their optical properties

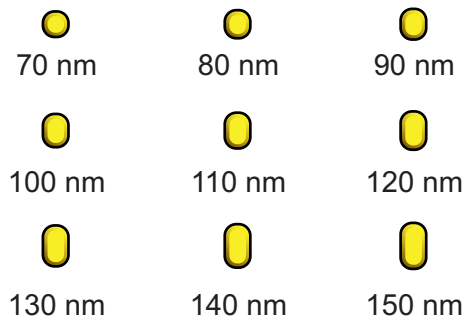


Figure 1.3: Lay-out of the plasmonic nanostructures. Nine nanorods with different lengths. Such structures have resonant plasmon modes at different, well-defined wavelengths.

by two independent methods using (1) dark field scattering spectroscopy and (2) spectroscopy of the intrinsic luminescence of the gold. Having characterized the plasmon modes, it was investigated whether the antennas enhance the chemiluminescence of lucigenin and hydrogen peroxide. In these experiments, no enhancement is observed. It was realized that for enhancement to occur, strict conditions must be met. For instance, the level of enhancement strongly depends on the emitter's location with respect to the antenna.

To prove that the structures are capable of enhancing emission, and to judge their performance, it was decided to perform a *fluorescence* enhancement experiment. A low-concentration fluorophore was allowed to diffuse through the near-field of the antenna. When monitoring the fluorescence intensity in time, sharp peaks are observed, which will be referred to as fluorescence bursts [8]. Here, we present a study of fluorescence bursts near different-sized antennas. We argue that the bursts can provide subdiffraction-limited information on spatially-varying enhancement near a nanostructure.

2 Chemiluminescence

Luminescence is a term used for the emission of light, which occurs when a quantum system (*f.i.* an atom or molecule) makes a jump between two states with different energies [6, 12]. The various types of luminescence differ by their mechanism to obtain the high energy state. For fluorescence, the energy is delivered by electromagnetic radiation (see Fig. 2.1c). For chemiluminescence, it is delivered by a chemical reaction (see Fig. 2.1b). The current section mainly describes chemiluminescence. For a review on fluorescence, the reader is referred to literature [13]. Section 2.1 describes the mechanism behind chemiluminescence. To illustrate the mechanism, the reader is introduced to the chemiluminescence reaction of lucigenin, which is used in this thesis. Section 2.2 describes the efficiency of chemiluminescence.

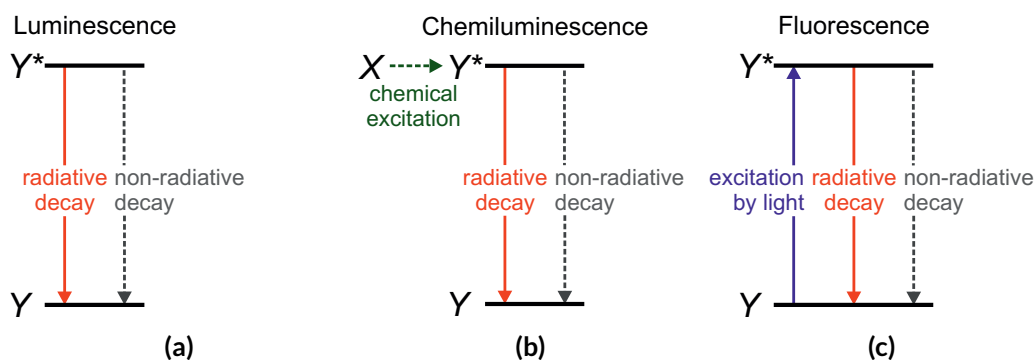


Figure 2.1: Simplified energy level diagrams for (a) luminescence in general, (b) chemiluminescence, and (c) fluorescence. Y is the ground state and Y^* the excited state. In (b), the excited state is produced by a chemical reaction. In (c), it is formed as the molecule absorbs electromagnetic radiation.

2.1 Mechanism of chemiluminescence

In a chemiluminescent process, a chemical reaction leads to a reaction product formed in an electronically excited state. Light is emitted when the molecule makes a transition to its ground state. To illustrate this, let us consider the chemiluminescent reaction of lucigenin and hydrogen peroxide (H_2O_2) used in this thesis. As shown in Fig. 2.2., lucigenin reacts with hydrogen peroxide to form N-methyl acridone (NMA) in the excited state. NMA can decay to its ground state with the emission of blue light. A base, *f.i.* sodium hydroxide (NaOH), is necessary to provide hydroxyl ions (OH^-).

If a second emitter is present in the chemiluminescent mixture, there can be energy transfer to that emitter, by a process called Förster resonance energy transfer (FRET). Chemiluminescence of this type is called indirect chemiluminescence. The reaction with lucigenin becomes indirect if lucigenin is present in a high concentration. In that case, the excited NMA

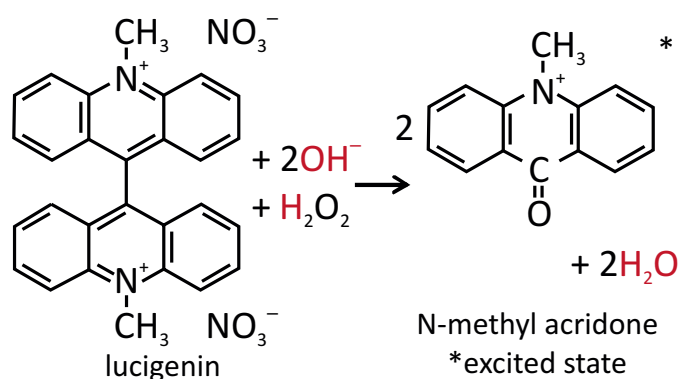


Figure 2.2: Reaction mechanism for the chemiluminescence of lucigenin.

can transfer its energy to the lucigenin. Lucigenin emits green light, so the observed color will change from blue to green.

In many chemiluminescent reactions a catalyst can be used to speed up the reaction. Catalysts are not consumed by the reaction. They provide a mechanism by which the reaction can occur that has a lower activation energy. Since the reaction rate depends exponentially on the activation energy, a slightly lower activation barrier can lead to a significant increase in reaction rate [14]. Since the chemiluminescence of luminol was first reported by Albrecht in 1928, several catalysts have been investigated, including metal ions and enzymes [15]. In 2005, Zhang *et al.* reported the use of gold nanoparticles to catalyze the reaction between luminol and hydrogen peroxide.

2.2 Efficiency of chemiluminescence

Chemiluminescence and fluorescence are both limited in efficiency because excited molecules can lose their energy through radiationless processes (*e.g.* internal conversion, intersystem crossing). Therefore, each excited molecule has a chance to decay radiatively *or* non-radiatively. These competing effects are usually described with decay rates. An initial population of excited molecules will decay radiatively at rate Γ_{rad} and non-radiatively at rate Γ_{nrad} . The total decay rate is given by

$$\Gamma_{tot} = \Gamma_{rad} + \Gamma_{nrad} \quad (2.1)$$

For a single excited molecule, the probability for radiative decay to occur is

$$\Phi_q = \frac{\Gamma_{rad}}{\Gamma_{tot}} \quad (2.2)$$

This expression is known as the quantum yield of the emitter. In Chapter 4, an explicit expression for Γ_{tot} will be given. It will be shown that in the presence of an antenna, the balance between the radiative and non-radiative rate can change.

Whereas the efficiency of a fluorescent process is usually assessed with the quantum yield, chemiluminescent processes are characterized by a different term: the chemiluminescence yield. This is the fraction of target molecules (to be detected) that eventually cause the emission of a photon: [16]

$$\Phi = \Phi_r \Phi_e \Phi_q \quad (2.3)$$

with Φ_r the fraction of target molecules that undergo a reaction, Φ_e the number of excited molecules formed per reaction, and Φ_q the quantum yield of the excited product as defined in Eq. 2.2. In case of indirect chemiluminescence, the chemiluminescence yield is defined differently:

$$\Phi = \Phi_r \Phi_e \Phi_t \Phi_q \quad (2.4)$$

where Φ_t is the efficiency of the energy transfer, and Φ_q is the intrinsic quantum yield of the new emitter.

3 Optical antennas

Antennas optimize the energy transfer between a localized source or receiver and the free-radiation field [17], as is shown in Fig. 3.1. This concept is widely used for radio- and microwaves, but it can be extended to the optical regime. The sources and receivers then become nano-scale objects, such as atoms and molecules. Optical antennas are usually based on metal nanostructures, which can confine fields beyond the diffraction limit. To understand their working, one needs to understand the optical properties of metals, which can be described with a frequency-dependent dielectric function (Section 3.1). Light with the right frequency can drive the free electron gas of a metal nanostructure into resonant oscillations. Resonant effects are most easily explained when the structure is much smaller than the wavelength of the light. This is known as the *quasi-static* approximation. Section 3.2 discusses resonant properties of a quasi-static sphere, such as enhanced scattering and absorption. Elongated structures require a different treatment, as is discussed in Section 3.3. In particular, it is shown that for elongated structures, the resonance wavelength becomes size-dependent.

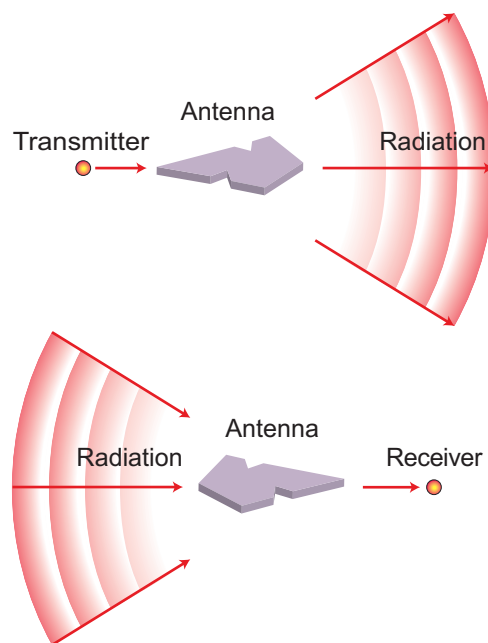


Figure 3.1: The concept of an antenna. (a) Transmitting antenna. (b) Receiving antenna. In the optical regime, the transmitters and receivers are nano-scale objects, such as atoms and molecules. Adapted from Novotny and van Hulst [17].

3.1 The complex dielectric function of metals

The optical properties of metals can be described using a frequency-dependent complex dielectric function $\epsilon(\omega)$. This function enters Maxwell's equations through the relation [18]

$$\mathbf{D} = \epsilon(\omega)\mathbf{E} \quad (3.1)$$

An approximate expression for $\epsilon(\omega)$ can be found using a Drude model, as is described in several texts, such as [18]. The result is

$$\epsilon_{Drude}(\omega) = 1 - \frac{\omega_p^2}{\omega^2 + i\Gamma\omega} \quad (3.2)$$

where Γ is a damping constant and ω_p is the plasma frequency, a natural frequency at which the electrons tend to oscillate [19]. The plasma frequency is given by $\omega_p = \sqrt{ne^2/(m_e\epsilon_0)}$ with n , e and m_e the density, charge, and effective mass of the free electrons.

For gold, this model gives accurate results in the infrared regime, but in the visible regime *interband transitions* should also be considered. In such a transition, a high-energy photon promotes an electron to the conduction band of the metal [18]. This can be pictured classically as oscillations of the bound electrons, induced by electromagnetic radiation. The contribution of a single interband transition is given by

$$\epsilon_{Interband}(\omega) = 1 + \frac{\tilde{\omega}_p^2}{(\omega_0^2 - \omega^2) - i\gamma\omega} \quad (3.3)$$

where $\tilde{\omega}_p$ is the plasma frequency for bound electrons, γ is a damping constant, and $\omega_0 = \sqrt{\alpha/m}$, with α the spring constant for the potential that keeps the electrons in place, and m the effective mass of the bound electrons.

One can model experimental data for $\epsilon(\omega)$ by adding contributions from the free-electrons (Eq. 3.2) and a single interband transition (Eq. 3.3). Fig. 3.2 shows a comparison with experimental data from Johnson and Christy for gold [20]. An offset $\epsilon_\infty = 6$ has been added to Eq. 3.3 to take into account all other interband transitions.

It is important to note from Fig. 3.2 that the real part of ϵ is negative. For this reason, the refractive index $n = \sqrt{\epsilon}$ will have a strong imaginary part. Therefore, electromagnetic fields can only penetrate the metal to a small extent. The length that the field penetrates is called the *skin depth*. Fig. 3.2 shows that as the wavelength increases, $\text{Re}(\epsilon)$ becomes more negative. For radio waves (~ 1 cm - 1 km), the skin depth is therefore negligible compared to the dimensions of an antenna. For light waves (~ 400 - 800 nm), however, $\text{Re}(\epsilon)$ is less negative. In that case, the skin depth is in the order of tens of nanometers [21], comparable with antenna dimensions. This means that fields penetrate the metal and cause oscillations of the free-electron gas. This is the topic of the next section.

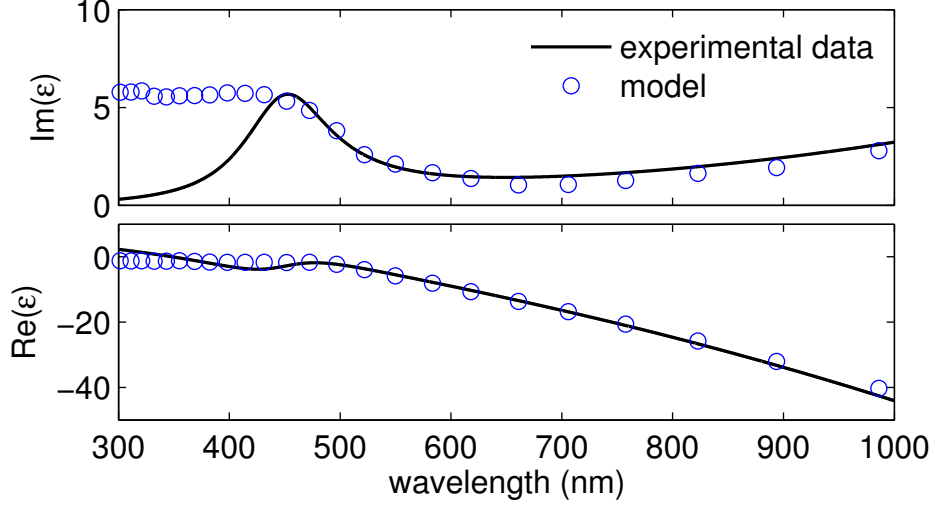


Figure 3.2: Experimental values [20] and model [18] for the dielectric function of gold. The model takes into account the contribution of free-electrons (Eq. 3.3) and one interband transition (Eq. 3.2). An offset $\epsilon_\infty = 6$ has been added to Eq. 3.3 to take into account all other interband transitions. The values used are $\omega_p = 13.8 \cdot 10^{15} s^{-1}$, $\Gamma = 1.075 \cdot 10^{14} s^{-1}$, $\tilde{\omega}_p = 45 \cdot 10^{14} s^{-1}$, $\gamma = 9 \cdot 10^{14} s^{-1}$, and $\omega_0 = 2\pi c/\lambda$, with $\lambda = 450$ nm.

3.2 Plasmonic resonances in quasi-static structures

When the electric field of a light wave penetrates a metal nanostructure, it drives the free electrons into a collective oscillation called a *surface plasmon* (SP) [22]. At certain frequencies, the oscillation is resonantly driven. Resonant effects in metal nanostructures are most easily explained for structures that are much smaller than the wavelength. In that case, the *quasi-static approximation* can be used. In this approximation, the applied field is considered to be uniform over the entire shape of the structure. It is only valid when the structure is smaller than the skin depth of the metal. In quasi-static structures, resonance effects can be found by solving for the electrostatic potential [22].

As an example, let us consider a metal sphere with dielectric function $\epsilon(\omega)$ in vacuum in a uniform field [18, 23, 24], which points in the x direction. The field will push positive charge to the "right" surface of the sphere, leaving a negative charge on the "left" surface [24]. By first solving for the electrostatic potential, one can obtain expressions for the fields in and outside the sphere:

$$\mathbf{E}_{in} = E_0 \frac{3}{\epsilon + 2} (\cos\theta \mathbf{n}_r - \sin\theta \mathbf{n}_\theta) \quad (3.4)$$

$$\mathbf{E}_{out} = E_0 (\cos\theta \mathbf{n}_r - \sin\theta \mathbf{n}_\theta) + \frac{\alpha}{4\pi\epsilon_0 r^3} E_0 (2\cos\theta \mathbf{n}_r + \sin\theta \mathbf{n}_\theta) \quad (3.5)$$

with α given by

$$\alpha = 4\pi\epsilon_0 a^3 \frac{\epsilon - 1}{\epsilon + 2} \quad (3.6)$$

Eq. 3.4 and 3.5 use spherical coordinates, with r the radial distance, θ the polar angle, and \mathbf{n}_r and \mathbf{n}_θ the corresponding unit vectors.

It should be noted that the second term in Eq. 3.5 is identical to the field of a dipole located at the center of the sphere. The dipole moment is given by $\mathbf{p} = \alpha \mathbf{E}$. It is important to study the form of α (Eq. 3.6). Whenever $|\epsilon + 2|$ has a minimum, resonant behavior occurs. One can distinguish three resonance effects:

1. *Enhanced local field.* The physical field near the sphere can be obtained by taking the real parts of Eq. 3.4 and 3.5. Fig. 3.3 shows the field distribution for a gold sphere at resonance (532 nm). Near the left and right surface, the field is resonantly enhanced. This can be seen from Eq. 3.5 by noting that, when taking the real part, α changes to $\text{Re}(\alpha)$. At resonance, $\text{Re}(\alpha)$ is very large, and therefore, so is $\text{Re}(\mathbf{E}_{out})$.

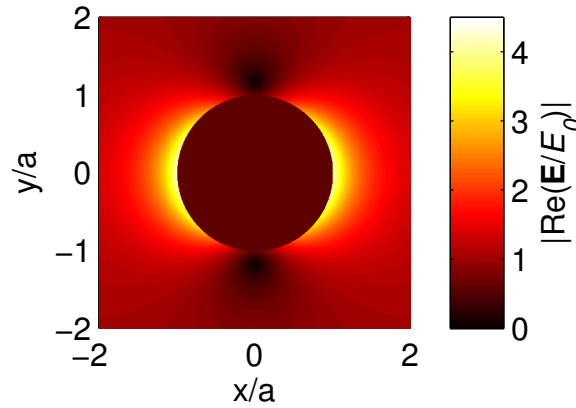


Figure 3.3: Field distribution near a gold sphere of radius a at the resonance wavelength (532 nm). Based on Eq. 3.4 and 3.5. $\epsilon = -4.60 + 2.44i$, in accordance to data from Johnson and Christy [20].

2. *Enhanced scattering.* Suppose the particle is illuminated by a plane wave, with a time-varying electric field. The induced dipole moment will also vary in time. The radiation of this dipole leads to scattering of the plane wave. For the scattering cross section one can derive

$$C_{sca} = \frac{k^4}{6\pi} |\alpha|^2 \quad (3.7)$$

with k the wavevector of the plane wave. At resonance, $|\alpha|$ is very large, so there will be enhanced scattering.

3. *Enhanced absorption.* Similar to the scattering cross section, one can define an absorption cross section:

$$C_{abs} = k \text{Im}(\alpha) \quad (3.8)$$

At resonance, $\text{Im}(\alpha)$ is also large, so there is enhanced absorption.

It should be noted that, for quasi-static structures, resonances are independent of particle size.

3.3 Plasmonic resonances in elongated structures

For elongated, rod-like particles, the applied field will differ in phase across the shape of the particle. In that case, the quasi-static approximation breaks down. The fields now create *propagating* SPs that reflect at the antenna ends, forming a Fabry-Perot resonator (Fig. 3.4). For a detailed treatment of propagating SPs, the reader is referred to [18]. Here, it is important to note that

1. The SP has a propagation constant $\gamma = \beta + \alpha i$, where β determines the SP wavelength ($\lambda_{SP} = 2\pi/\beta$), and α accounts for damping of the SP.
2. The SP penetrates into the surrounding medium. This leads to an additional phase Φ that is picked up upon reflection at the antenna ends.

This description is summarized in Fig. 3.4. The figure shows the phase contributions that the SP acquires as it travels back and forth a cylindrical rod. The condition for a Fabry-Perot resonance is [25]:

$$\beta L_{res} + \Phi = n\pi \quad (3.9)$$

with L_{res} the resonance length of the rod and n the order of the resonance ($n = 1, 2, \dots$). The resonance length of the first order is then

$$L_{res} = \pi/\beta - \Phi/\beta \quad (3.10)$$

From a similar model by Novotny [2], we note that the second term can be approximated by $2R$, where R is the radius of the rod. One then obtains

$$L_{res} = \pi/\beta - 2R \quad (3.11)$$

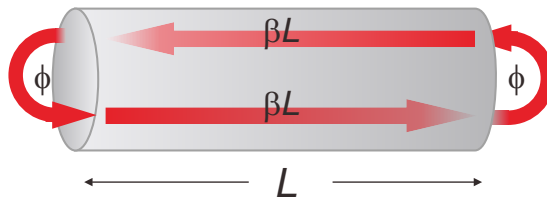


Figure 3.4: Schematic picture of an SP propagating back and forth a cylindrical rod. Between the two ends, the SP acquires a phase βL . At each reflection, it picks up an additional phase Φ . Image adapted from Biagioni, Huang and Hecht [25].

As mentioned above, β is the real part of the propagation constant γ . To determine γ , it is necessary to calculate the modes of an infinite cylindrical waveguide. The TM_0 modes are solutions to the equation [2, 26]

$$\frac{\epsilon(\lambda) J_1(\kappa_1 R)}{\kappa_1 R J_0(\kappa_1 R)} - \frac{\epsilon_s H_1^{(1)}(\kappa_2 R)}{\kappa_2 R H_0^{(1)}(\kappa_2 R)} = 0 \quad (3.12)$$

with $\kappa_1 = k_0 \sqrt{\epsilon(\lambda) - (k_0/\gamma)^2}$, and $\kappa_2 = k_0 \sqrt{\epsilon_s - (k_0/\gamma)^2}$.¹ Here, $\epsilon(\lambda)$ is the dielectric function of the metal, ϵ_s is the dielectric constant of the surrounding medium, and R is the radius of the cylinder. Furthermore, J_n and $H_n^{(1)}$ are Bessel and Hankel functions of the first kind.

Fig. 3.5 shows how the resonance length depends on the free-space wavelength. The curve was calculated using Eq. 3.11, where $\beta = \text{Re}(\gamma)$ was obtained by solving Eq. 3.12 numerically using a minimization algorithm². Traditional antennas have a length that is half the free-space wavelength. As the figure shows, optical antennas have a length that is a factor 2-5 shorter. In many texts, it is said that the antenna does not respond to the free-space wavelength, but to a shorter *effective wavelength* [2]. The relation between the antenna length and the effective wavelength is

$$L_{res} = \lambda_{eff}/2 \quad (3.13)$$

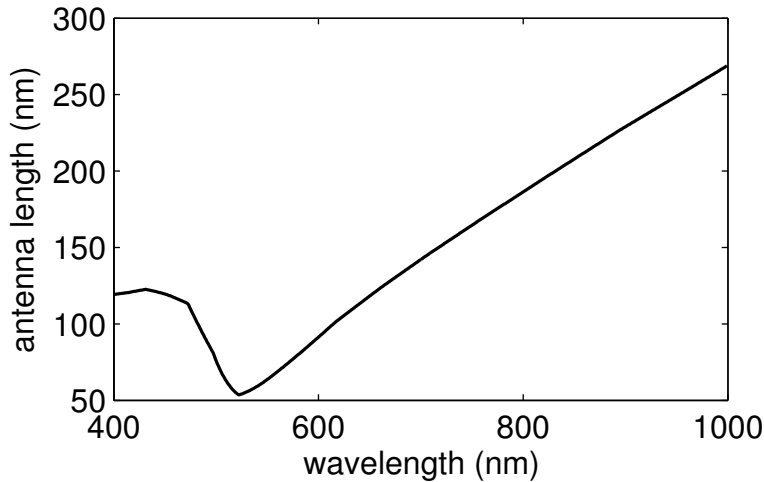


Figure 3.5: Resonant lengths for gold rods with radius $R = 20$ nm, as a function of the free-space wavelength. The curve was calculated using Eq. 3.11, where $\beta = \text{Re}(\gamma)$ was obtained numerically using Eq. 3.12. Experimental values for ϵ were used [20]. The curve is closely related to the effective wavelength curve from Novotny [2], according to Eq. 3.13.

¹When taking the square root in these expressions, one finds two values. For κ_2 , the value with positive imaginary part must be taken [26].

²Although there are approximate expressions to calculate L_{eff} , these are only valid for very thin antennas ($R \ll \lambda$). The antennas used in this thesis have radius $R \approx 35$ nm. To find the theoretical resonance wavelengths of these antennas, it is more accurate to use Eq. 3.11 and 3.12.

4 Luminescence near optical antennas

Many studies show enhanced fluorescence near metal nanoparticles [8, 9]. The enhancement is based on two factors. On the one hand, there is enhanced *excitation* due to the strong electric field near the antenna (see Section 3.2), which leads to a higher absorption rate of the fluorophore. On the other hand, as will be explained, there can be enhanced *emission* due to the optimized nanophotonic environment. In case of chemiluminescence, there is *chemical* rather than optical excitation (see Section 2.1). Therefore, enhanced excitation does not play a role, and will not be discussed. Instead, the current section describes enhanced emission. Section 4.1 shows how the presence of an antenna can change the balance between radiative and non-radiative decay. It will turn out that antennas either increase or decrease the quantum yield. Section 4.2 presents a model for this behavior. This chapter ends with a literature overview on enhanced chemiluminescence (4.3).

4.1 Radiative and non-radiative decay near an antenna

The *total* decay rate of a quantum emitter in a dissipative environment can be determined using *Fermi's golden rule*, giving [7, 21]:

$$\Gamma_{tot}(\omega, \mathbf{r}, \mathbf{e}_d) = \frac{\pi d^2 \omega}{\hbar \epsilon_0} N(\omega, \mathbf{r}, \mathbf{e}_d) \quad (4.1)$$

with ω the emission frequency, \mathbf{r} the position of the dipole, \mathbf{e}_d a unit vector indicating the dipole orientation, and d the modulus of the matrix element for the transition. $N(\omega, \mathbf{r}, \mathbf{e}_d)$ is the *local density of optical states* (LDOS). Eq. 4.1 can be decomposed into two parts. One part accounts for the intrinsic quantum properties of the source through the transition matrix element d . The other part accounts for the environment of the emitter through the LDOS.

By changing an emitter's environment, one can increase the LDOS and thereby, through Eq. 4.1, the total decay rate. The presence of an antenna leads to a higher LDOS because photons can be emitted through the modes of the antenna. However, some of these photons are lost because they excite higher order non-radiative modes. This means that the antenna not only increases the radiative decay rate, but also the non-radiative rate. For enhancement in intensity to occur, the increase of the radiative decay rate needs to be *higher*.

One can establish a classical analogue by noting that the LDOS can be expressed as

$$N(\omega, \mathbf{r}, \mathbf{e}_d) = \frac{6\omega}{\pi c^2} (\mathbf{e}_d^T \cdot \text{Im}(\mathbb{G}(\mathbf{r}, \mathbf{r}, \omega)) \cdot \mathbf{e}_d) \quad (4.2)$$

where \mathbb{G} is the *Green dyadic* of the electromagnetic problem, which represents the response

of a dipole to the local environment. In Eq. 4.2, \mathbb{G} is evaluated at the location of the emitter itself. This reveals the fact that the decay happens in response to the emitter's own field. When placed near an antenna, a classical dipole will experience a driving force from its own secondary field - the field scattered from the antenna and arriving back at the dipole's position. On the one hand, the dipole's power may increase, due to constructive interference with the secondary field. On the other hand, the dipole's power will be decreased due to absorption by the antenna.

4.2 Model for enhancement

The previous section showed how an antenna can increase both the radiative and non-radiative decay rate of an emitter. Whether intensity enhancement occurs, depends on the balance between the two. The current section presents a model for this behavior. The model is based on a dipole emitter near a spherical antenna [21, 27] like the one in Section 3.2, in air. The intrinsic quantum yield of the emitter is denoted as

$$\Phi_q^0 = \frac{\Gamma_{rad}^0}{\Gamma_{rad}^0 + \Gamma_{nrad}^0} \quad (4.3)$$

In the presence of the sphere, there will be a new quantum yield:

$$\Phi_q = \frac{\Gamma_{rad}}{\Gamma_{rad} + \Gamma_{nrad}} \quad (4.4)$$

However, as explained in Section 4.1, the antenna introduces a new loss channel, due to non-radiative energy transfer to the antenna. Therefore, the non-radiative decay rate is split in two:

$$\Gamma_{nrad} = \Gamma_{abs} + \Gamma_{nrad}^0 \quad (4.5)$$

Combining Eq. 4.3, 4.4, and 4.5, one obtains

$$\Phi_q = \frac{\Gamma_{rad}/\Gamma_{rad}^0}{\Gamma_{rad}/\Gamma_{rad}^0 + \Gamma_{abs}/\Gamma_{rad}^0 + [1 - \Phi_q^0]/\Phi_q^0} \quad (4.6)$$

To determine Φ_q , one needs to find expressions for $\Gamma_{rad}/\Gamma_{rad}^0$ and $\Gamma_{abs}/\Gamma_{rad}^0$. For a derivation, the reader is referred to [21, 27]. Here, we will only state the expressions and note their consequences.

$$\frac{\Gamma_{rad}}{\Gamma_{rad}^0} = \left| 1 + 2\tilde{\alpha} \frac{a^3}{(a+z)^3} \right|^2 \quad (4.7)$$

$$\frac{\Gamma_{abs}}{\Gamma_{rad}^0} = \frac{3}{4} \text{Im} \left[\frac{\epsilon - 1}{\epsilon + 1} \right] \frac{1}{(kz)^3} \quad (4.8)$$

Here, a is the radius of the sphere, z is the distance between the emitter and the surface of the sphere, ϵ is the dielectric function of the metal (see Section 3.1), and $\tilde{\alpha} = \alpha 4\pi\epsilon_0 a^3$ with α

the polarizability of the sphere as in Eq. 3.6 (Section 3.2).

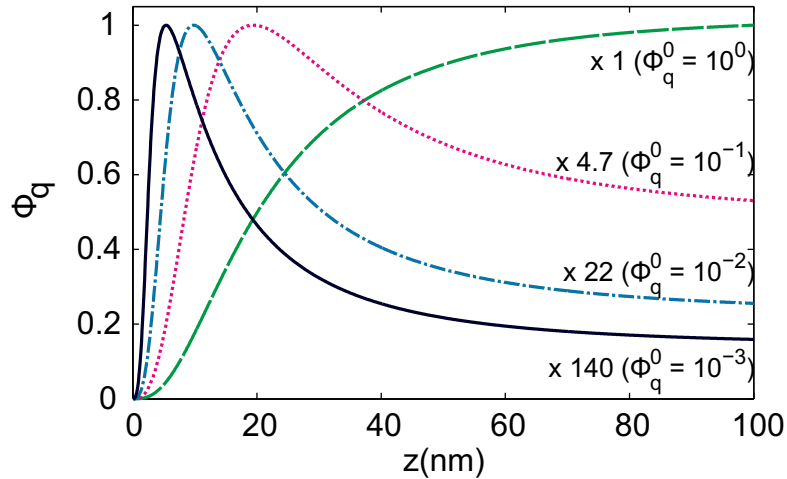


Figure 4.1: Quantum yield of an emitter near a gold sphere, as a function of their separation distance, for emitters with different intrinsic quantum yields (Φ_q^0). The sphere has radius $a = 40$ nm, and $\epsilon = -9.30 + 1.54i$, in accordance to data from [20] at 600 nm. The curves are scaled to the same maximum value. Based on the model by Bharawaj and Novotny [21, 27].

Using Eq. 4.7, 4.8, and 4.6, one can calculate the quantum yield. Fig. 4.1 shows the result for a gold sphere with a radius of 40 nm. The figure shows that when the intrinsic quantum yield $\Phi_q^0 = 1$, the antenna can only reduce the quantum yield. Furthermore, whether enhancement occurs strongly depends on the distance z . For too large distances, there is no interaction between the emitter and the antenna, and the quantum yield is unchanged: *i.e.* $\Phi_q = \Phi_q^0$. For too small distances, energy dissipation dominates, and the quantum yield decreases: $\Phi_q < \Phi_q^0$.

Finally, it should be noted that the highest enhancement does not occur at the plasmon resonance frequency. In fact, it occurs at a frequency that is shifted to the red part of the spectrum. This can be explained by studying the resonances of Eq. 4.7 and 4.8. Eq. 4.7, which characterizes radiative decay, has a resonance governed by the denominator of $\alpha (\epsilon + 2)$. This is the familiar plasmon resonance (see Section 3.2). Eq. 4.8, which characterizes absorption, has a different resonance, governed by $\epsilon + 1$. Although there is increased emission at the plasmon resonance, this effect is strongly attenuated by resonant absorption at a nearby frequency (blue-shifted compared to the plasmon resonance). Therefore, maximum enhancement occurs at a red-shifted frequency, where the absorption plays a smaller role. The gold sphere presented here has a maximum enhancement around 667 nm.

4.3 Plasmon-enhanced chemiluminescence

In 2006, it was reported that chemiluminescence on a silver island film shows a 20-fold increase in intensity [10]. This increase is not attributed to a catalytic effect, but to surface plasmons. In 2007, a similar experiment was done where the silver film lays on top of a prism [11]. The group reports highly directional and polarized emission of the luminescence from the prism side. This implies that the luminescence excites plasmons in the silver film, which couple out through the prism. In enhanced fluorescence plasmonic effects can always be verified by direct measurement of the increase in radiative decay rate. For chemiluminescence such rates can not be measured because chemical reactions occur randomly and cannot be synchronized. A clear separation of the enhancement of the chemical reaction speed and the enhanced radiative quantum yield is therefore difficult to obtain experimentally.

5 Experimental aspects

To be able to study chemiluminescence in a system with well-defined resonances, an array of nanostructures was developed. Section 5.1 presents the design of these structures and explains how they were fabricated. Based on scanning electron microscope (SEM) images, the quality of the fabricated structures is discussed. The experiments in this thesis were done using two experimental setups: a dark field setup and a fluorescence microscope. These are described in Sections 5.2 and 5.3.

5.1 Antenna sample

5.1.1 Design and fabrication

To compare the behavior of antennas with different resonances, 3x3 array of gold nanorods was designed (Fig. 5.1). While the antennas have the same width and depth (~70 nm and ~30 nm, respectively), their length increases (~70-150 nm). The structures were fabricated by focused ion beam (FIB) milling in a gold flake. To achieve this, single crystalline gold flakes were chemically synthesized and cast onto a glass cover slip (1x1 inch, no. 1.5). As a scanning electron microscope (SEM) was used for inspection, the flake samples were coated with a thin conducting layer (gold for one sample and gold-palladium for another; see below). This layer is necessary because glass substrates tend to charge during SEM-inspection, leading to distorted images. Finally, the antenna array was formed by FIB milling in one of the flakes.

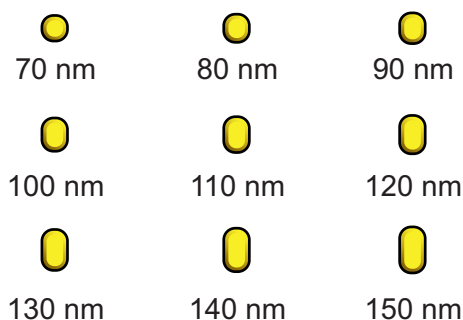
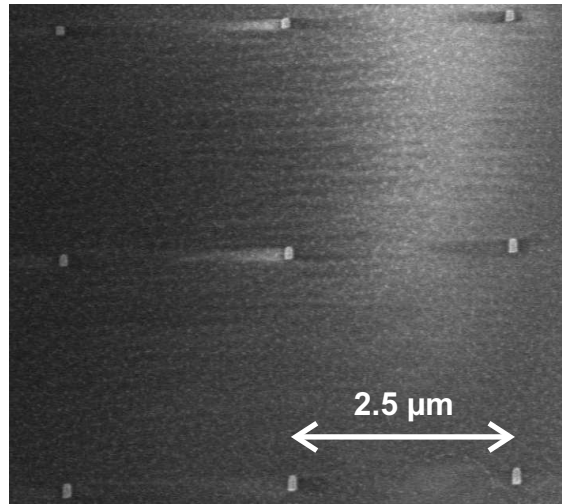


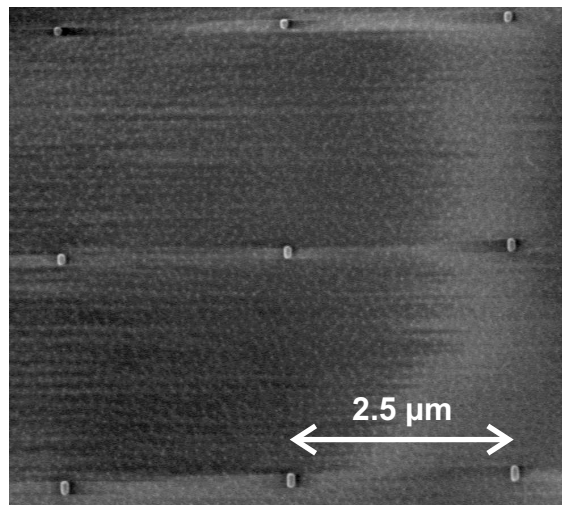
Figure 5.1: Design of the plasmonic nanostructures. Nano-antennas with different lengths (~70-150 nm), but the same width (~70 nm) and depth (~30 nm).

The experiments in this thesis were done using two samples¹. These will be referred to as Sample 1 and Sample 2. Although the samples have the same design, there were some differences in the fabrication procedure. For one, the gold flakes were synthesized using a different recipe. The flake used for Sample 1 was relatively thick (~63 nm) and had to be thinned

¹The initial sample broke, so a new one had to be fabricated.



(a) Sample 1



(b) Sample 2

Figure 5.2: Scanning electron microscope images of the plasmonic structures. (a) Sample 1. (b) Sample 2.

down significantly to obtain an antenna depth of ~30 nm. The flake for Sample 2 was ~42 nm thick, which required less thinning. Furthermore, a different conducting layer was used for each sample: a 10 nm gold layer for Sample 1, and a 5 nm gold-palladium layer for Sample 2.

5.1.2 Scanning electron microscope inspection

The quality of the structures will now be judged using scanning electron microscope (SEM) images of Sample 1 and Sample 2 (Fig. 5.2a and 5.2b). Some parts of the SEM images are brighter than others, e.g. the bright area in the north-east corner of Fig. 5.2a. This is ascribed to charging of the glass substrate. We note that in both images, the nine antennas can be clearly distinguished. The distance between them is 2.5 μm , which is considered to be large enough to avoid interaction between the antennas. Looking at the shapes of the nine antennas, it can be seen that the width stays approximately constant, while length gradually increases, as was intended in the design. For instance, the antenna in the upper-left corner is roughly square, while the antenna in the bottom-right corner is elongated. The area between the antennas seems to be fairly flat, except for some graininess. It is expected that this graininess was caused while milling into the glass.

5.1.3 Sample cleaning

The sample was exposed to various chemicals. As the sample needed to be re-used, it was cleaned after every experiment. This was done by immersing the sample in water and by flowing some methanol over the top and bottom surface. Finally, the sample was placed in an ozone cleaner for 30 minutes (*BioForce Nanosciences, UV/Ozone Pro Cleaner Plus*). At the end of the thesis, a comparison was made between methylene blue fluorescence on a regular empty cover slip and a *cleaned* empty cover slip. The methylene blue showed less counts on the cleaned cover slip. A possible cause is that on a clean surface, the liquid tends to spread, forming a thin layer.

5.2 Dark field characterization setup

5.2.1 Experimental setup

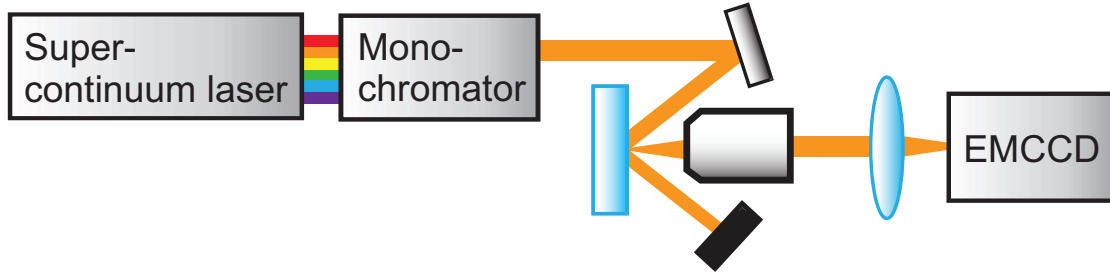


Figure 5.3: Schematic overview of the dark field characterization setup.

A common way to characterize the plasmon modes of a nanostructure is to illuminate it with a plane-wave and study the scattered far-field [28]. To characterize multiple structures, it is usually required to illuminate them one by one. However, the Optical Sciences group has developed a method to study many structures in parallel. The experimental setup is based on a dark field configuration, as shown in Fig. 5.3. In this geometry, the transmitted and reflected beams are rejected by angular separation, so that only scattered light is collected. In our method, the samples are illuminated using a spectrally filtered white light continuum laser (Fianium SC400-4; 4 W; 40 MHz repetition rate). A single wavelength is selected using a monochromator (Acton SP2150i). A $50 \times 50 \mu\text{m}^2$ area (potentially containing 400 separate nanostructures) is then imaged on an EMCCD (Andor iXon3 897) for many different wavelengths (400-1000 nm). To compensate for chromatic aberration, the sample is moved using a computer-controlled stage following a fitted curve.

5.2.2 Typical dark field spectrum

In this section, it is shown how the dark field setup was used to obtain the scattering spectrum of an individual antenna. The excitation beam was polarized parallel to the long axis of the antennas to make sure that only the mode along the long axis was excited. The dark field setup produces hyperspectral images from which per-pixel spectra can be constructed. Fig. 5.4 shows dark field images of Sample 1 at four separate wavelengths. An individual spectrum is based on the average intensity of a 10×10 pixel area around an antenna. It is necessary to subtract a background spectrum, based on a 8×8 pixel area of the glass surface. It is important to note that the spectra are corrected for the wavelength-dependent sensitivity of the setup, also known as the system response function. The wavelength-dependence is *f.i.* caused by the wavelength-dependent laser intensity and EMCCD sensitivity. To correct for this, the spectra were divided by a calibration curve (Fig. 5.5), measured by recording the dark field spectrum of a diffuser element, which causes uniform scattering.

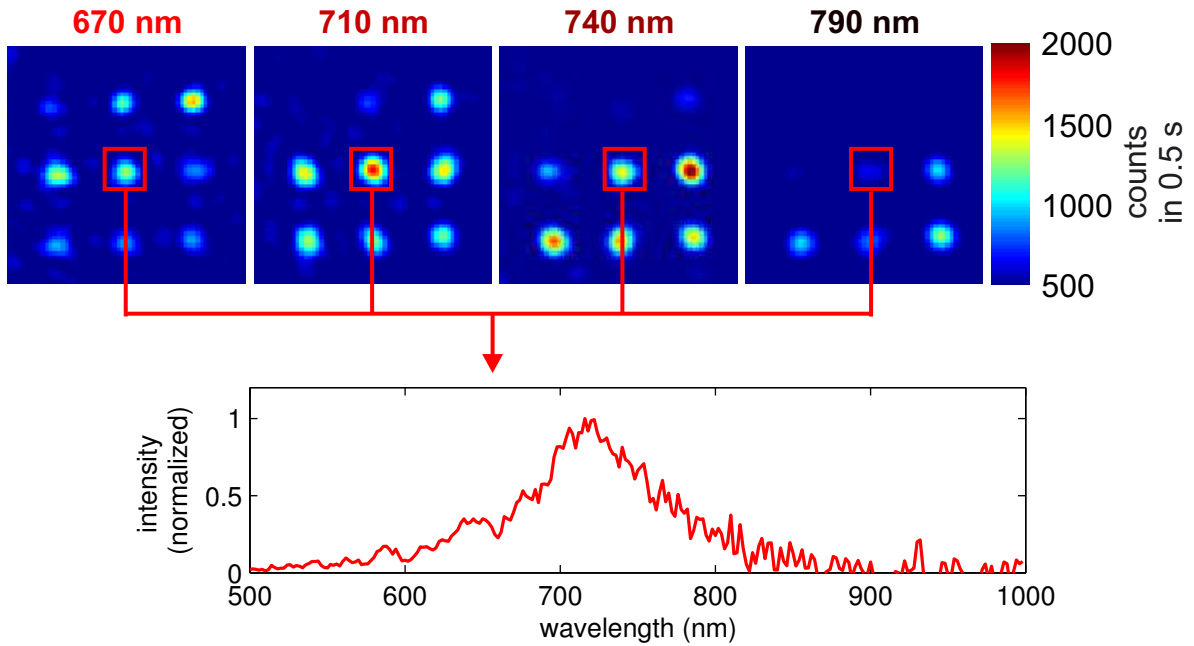


Figure 5.4: Procedure to obtain individual antenna spectra from the dark field images.

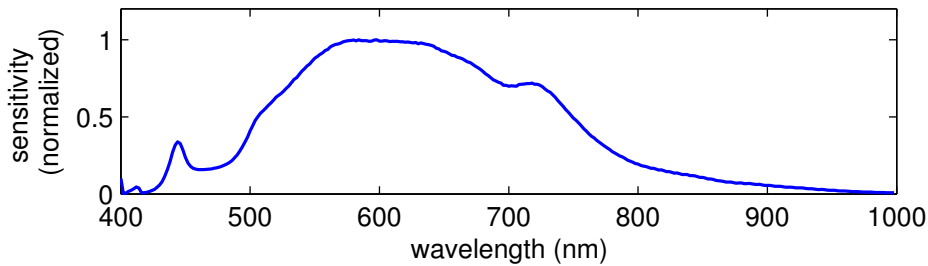


Figure 5.5: Spectral sensitivity of the dark field setup.

It should be noted that Fig. 5.4 shows negative counts above 900 nm. The reason is that at a few wavelengths, the subtraction of the background led to a small negative number. This negative number was then multiplied by a large number to correct for the low system response function above 900 nm.

5.3 Fluorescence microscope

5.3.1 Experimental setup

Fluorescence and chemiluminescence can be detected using a fluorescence microscope, as shown in Fig. 5.6. As described in [29], the excitation beam is produced by a white light continuum laser (Fianium SC 400-2-PP; 2 W; 20 MHz repetition rate). The excitation wavelength is selected using an acousto-optic tunable filter (AOTF). The beam is coupled into a single-mode fibre by one objective (Olympus Plan Achromat, 10x, 0.25 NA) and coupled out by an-

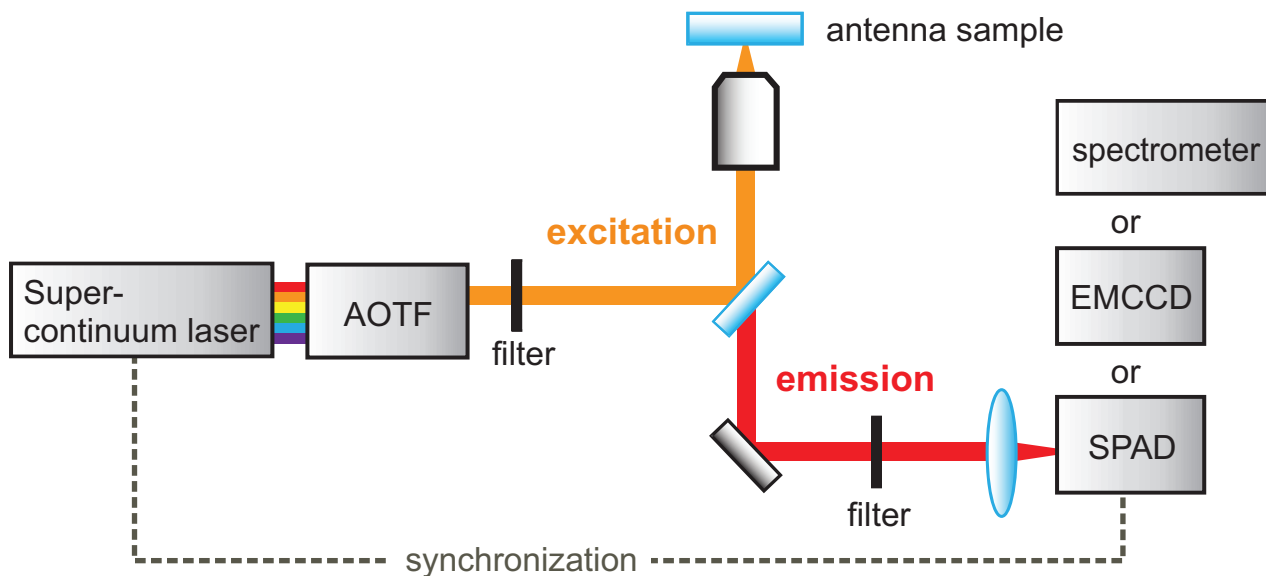


Figure 5.6: Schematic overview of the fluorescence microscope.

other (Olympus Plan Achromat, 4x, 0.10 NA). Next, it is passed through a filter to block any wavelengths other than the excitation wavelength. In the experiments in this thesis different filters were used, as described in Appendix A. After the filter, the beam enters an Olympus IX71 inverted microscope. There, it is directed up via a wedged beam splitter and focused on the sample using an oil-immersion objective (Olympus UPlanSApo, 100x, 1.40 NA). The position of the cover-slip is controlled using an XYZ piezo scanning stage (PI P-527.3 CD), operated by a piezo-controller (PI E-710). As shown in the figure, light emitted by the sample is picked up by the same objective. It passes through the beam splitter and is directed out of the microscope by a mirror. Next, it is passed through a filter to eliminate the excitation light. Finally, the light is focused onto a Single Photon Avalanche Diode or SPAD (PicoQuant MPD-SCTC). The signal from the SPAD is read by a single-photon computer card (Becker-Hickl SPC-830) with a detection window of 50 ns divided in 4096 bins. By using flip-mirrors, it is possible to direct the light towards an EMCCD or spectrometer instead of the SPAD.

5.3.2 Typical gold luminescence spectrum

This section shows how the fluorescence microscope was used to obtain spectra of the intrinsic luminescence of the antenna material (gold). The excitation was polarized along the *short* axis of the antennas, which has the same size for each antenna. In the other direction, the antennas have different sizes. When exciting in the long direction, some antennas would be more resonant than others. As a result, some antennas would be excited by a higher field, which hinders a fair comparison.

Fig. 5.7 shows the gold luminescence spectrum for the 140 nm antenna. Let us first consider the shape of the black curve, which shows the spectrum obtained when no polarizer is

present in the detection pathway. The spectrum shows a sharp rise at 633 nm. This is due to the 633 long-pass filter in the emission pathway. Furthermore, the spectrum shows two major peaks. These peaks appear because the luminescence is preferentially emitted through the two modes of the antennas: the mode along the horizontal axis and the mode along the vertical axis. The peak at ~ 800 nm is quickly attenuated above ~ 820 nm. The reason is that high wavelengths are not efficiently detected in the setup, as was briefly checked by looking at the spectrum of a broadband source. It is desirable to correct for this, using a system response function, as was done for the dark field setup (Section 5.2). Such a function is however hard to determine, because it requires a sample with a flat luminescence spectrum. For a layer of bulk gold, the luminescence spectrum is broadband, but not flat. The spectrum will show a plasmon peak depending on the thickness of the layer.

Let us now discuss the effect of placing a polarizer in the detection pathway. Fig. 5.7 shows the gold luminescence spectrum for the 140 nm antenna. Without a polarizer (solid black line), the spectrum has two peaks, because photons are emitted through the plasmon modes along the short *and* long axis. These two modes are perpendicularly polarized. Therefore, by using a polarizer, one can select the "short mode" (dotted pink line) or the "long mode" (dash-dotted blue line). In this thesis, we are interested in the long mode.

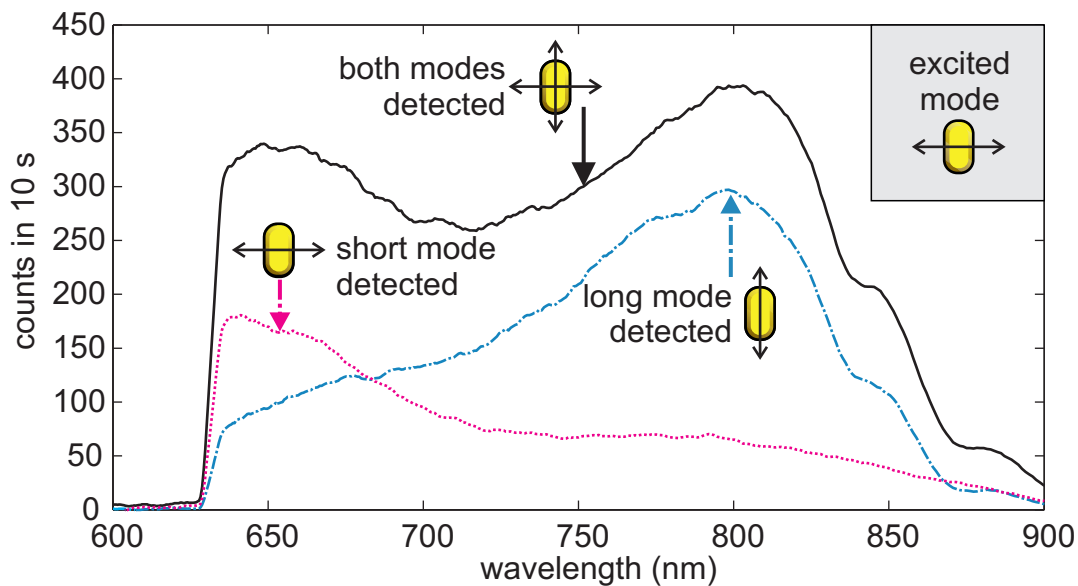


Figure 5.7: Measured gold luminescence spectra in water for the 140 nm antenna. Without filtering on polarization, two antenna modes are observed. With a polarizer, the mode along the short or the long axis can be selected.

5.3.3 Typical fluorescence time trace

Here, it is shown how the setup can be used to obtain a fluorescence time trace. With the SPAD, a microtime and macrotime are stored for each photon. The microtime is the time delay between an excitation pulse and the detection event. The macrotime is the time between the start of the measurement and the detection event. A time-trace of the fluorescence intensity can be obtained by dividing the macrotimes into bins of a certain time interval, e.g. 10 ms. The number of photons in each bin is a measure for the intensity during that interval. In other words, a histogram of macrotimes shows the fluorescence intensity as a function of time. Fig. 5.8 shows an example of a fluorescence time trace using a 10 ms bin time.

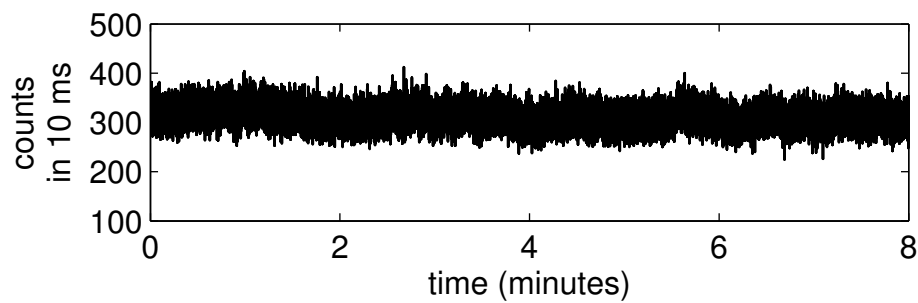


Figure 5.8: Typical time trace obtained with the fluorescence microscope. The bin time is 10 ms. The trace was measured near the 100 nm antenna in water.

6 Results and discussion

The primary experimental results of this thesis are a study on lucigenin chemiluminescence and a study on methylene blue fluorescence near different-sized antennas. To check whether the antenna modes show spectral overlap with these emitters, the modes were characterized by looking at 1) dark-field scattering (Section 6.1), and 2) intrinsic luminescence of the gold (Section 6.2). To judge the accuracy of the measured resonances, they are compared to values predicted by a model for cylindrical antennas (Section 6.3). The influence of the antennas on lucigenin chemiluminescence is presented in Section 6.4. The chemiluminescence has two emitting components: 1) N-methyl acridone, and 2) the lucigenin itself, excited by N-methyl acridone through Förster resonance energy transfer. The emission of the second component was studied first, with excitation by light. Following this, the complete chemiluminescent system was studied. We show that the antennas in fact *darken* the emission, and explore several explanations. To aid the discussion, antenna enhancement was tested in a more controlled study, by monitoring fluorescence time-traces of methylene blue diffusing through an antenna's near-field (Section 6.5). As a novel tool to analyze these time traces, we propose the use of photon count histograms.

6.1 Dark field scattering spectra

To find the resonance wavelengths of the antennas, dark field scattering spectra were measured using the setup described in Section 5.2. The spectra are shown in Fig. 6.1. From the figure, it is noted that each spectrum has one significant peak. Also, the longer the antenna, the higher the peak wavelength. Finally, it is noted that the spectra of longer antennas show higher intensities.

Discussion

The peaks in the scattering spectra are expected, because nanostructures show enhanced scattering at the plasmon resonance (see Section 3.2). The peaks therefore indicate the resonance wavelengths of the antennas. It is also expected that the resonance wavelength is higher for longer antennas (see Section 3.3). The observation that longer antennas scatter with a higher intensity can be explained by considering the scattering cross section. For a spherical particle, this cross section scales with the radius cubed (a^3), as can be seen by combining Eq. 3.7 and 3.6.

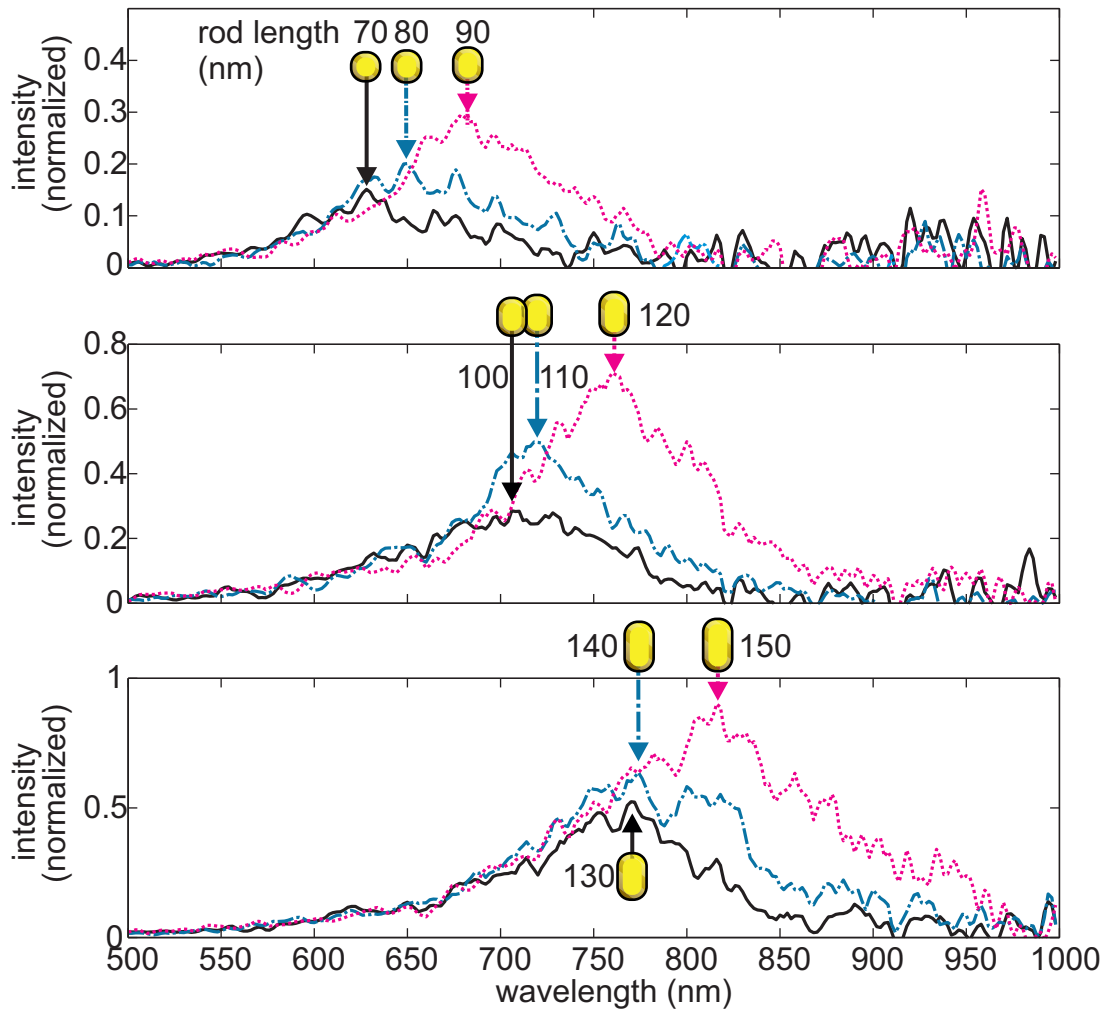


Figure 6.1: Measured dark field scattering spectra for 70-150 nm antennas in air. A moving average involving 3 datapoints (6 nm) was taken to smooth the curves.

6.2 Gold luminescence spectra

The resonance wavelengths were obtained in an alternative way using the intrinsic luminescence of the antenna material (gold). Fig. 6.2 shows the luminescence spectra for each individual antenna. Only the modes parallel to the long axis were transmitted to the detector. Again, each spectrum has a single peak. In most cases, the longer antennas have a peak at a higher wavelength. It should be noted that the spectra of the 140 and 150 nm antennas show a decreased intensity.

Discussion

The peaks in the spectra arise because there is preferential emission through the plasmon modes of the antenna. The peaks should therefore correspond to the resonance wavelengths of the antennas. The spectra of the 140 and 150 nm antennas have a lower intensity because the setup has a lower sensitivity at high wavelengths (see Section 5.3). The figure also shows the measured fluorescence spectrum of methylene blue (light gray) and chemiluminescence spectrum of lucigenin (dark gray). The lucigenin spectrum has a peak around 500 nm, which is not shown. Only the tail, which extends beyond 640 nm, is visible. The methylene blue spectrum peaks around 675 nm, *i.e.* between the peaks corresponding to the 80 and 90 nm antennas.

Judging from the figure, the lucigenin spectrum is closest to the spectrum of the 70 nm antenna. It is expected that this antenna shows most enhancement. The methylene blue spectrum seems closest to the spectra of the 80 and 90 nm antennas. As a more quantitative measure, for each antenna an overlap integral with the methylene blue spectrum was calculated. The values of the integrals are shown in Fig. 6.3. Based on this figure, the 80 and 90 nm antennas have most overlap. For methylene blue, these antennas are expected to cause most enhancement.

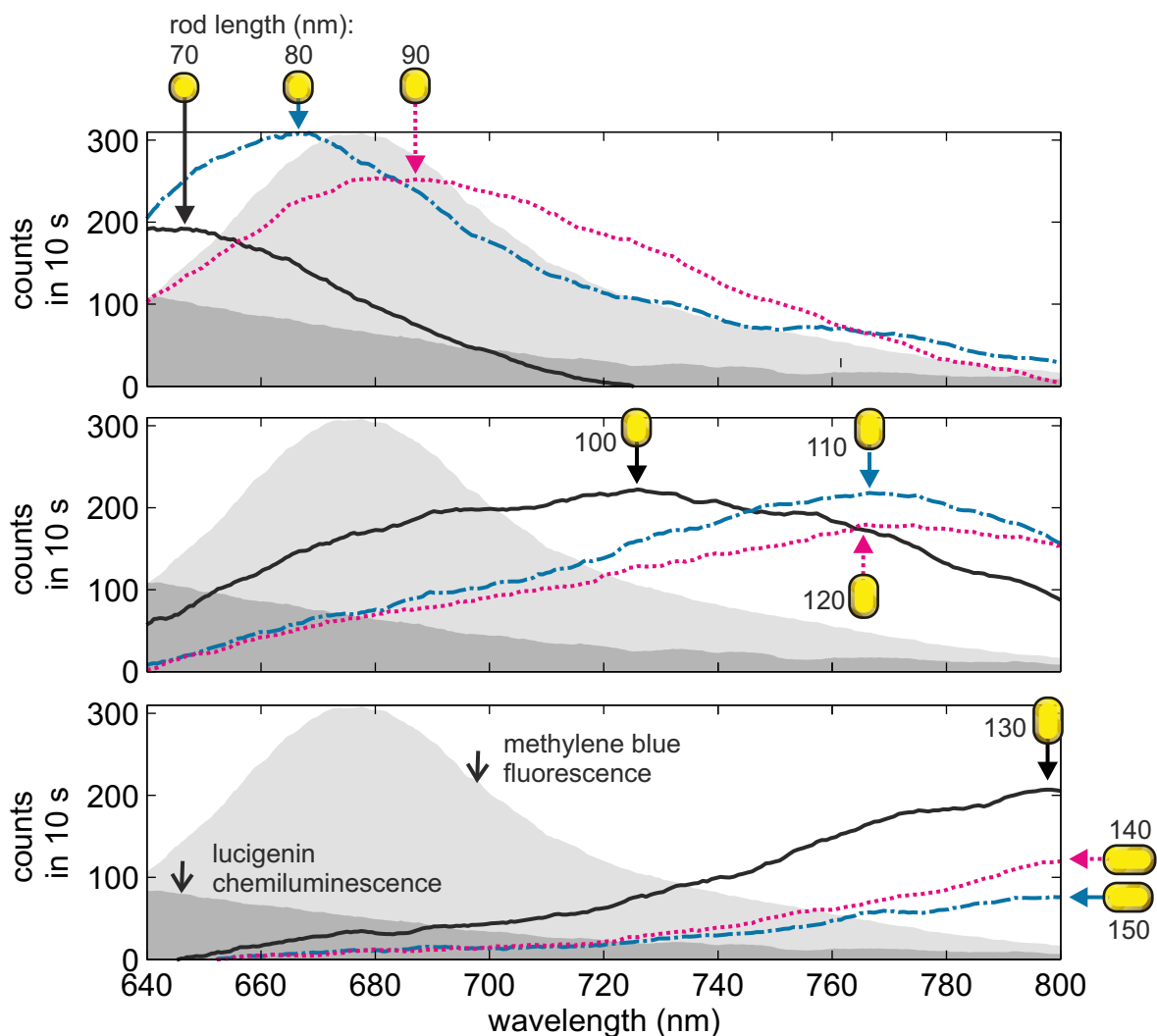


Figure 6.2: Measured gold luminescence spectra for 70-150 nm antennas in water. In the background, the chemiluminescence spectrum of lucigenin (dark gray) and the fluorescence spectrum of methylene blue (light gray) are shown. All spectra except the methylene blue spectrum were smoothed using a moving average involving 13 data points (~6 nm).

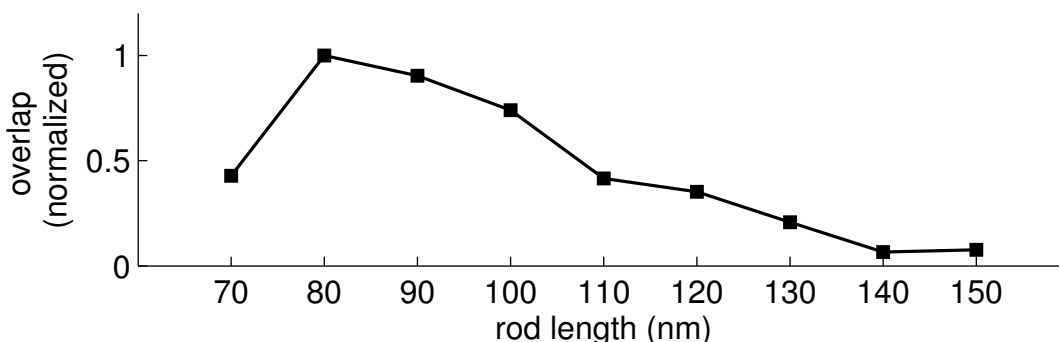


Figure 6.3: Calculated overlap between the gold luminescence spectra and the emission spectrum of methylene blue.

6.3 Resonances compared to theory

To judge the accuracy of the measured resonances, the dark field peaks and gold luminescence peaks will now be compared. Besides, they will be compared to values predicted by theory. From each dark field spectrum and gold luminescence spectrum, a peak wavelength was extracted. Fig. 6.4 shows the relation between the peak wavelengths and the antenna lengths. The antenna lengths were estimated to have a 10 nm inaccuracy due to the fabrication process. It should be noted that the luminescence peaks (right panel) corresponding to the 130-150 nm antennas are omitted because the setup is not sensitive enough in the high wavelength region (see Section 5.2).

The figure also shows the theoretical relation between resonance wavelength and antenna length. These relations were calculated using the model for cylindrical rods described in Section 3.3. Because the structures in our experiment are not cylinders, but bars, each panel shows two lines. The first line corresponds to a cylinder with a 15 nm radius (half the antenna depth). The other line corresponds to a cylinder with a 35 nm radius (half the antenna width). The area between these two lines has been shaded.

As the antennas lay on a glass substrate, they are not surrounded by a single medium, but by two media. To take this into account, the average refractive index of the two media was taken, *i.e.* the average of glass and air (~ 1.25) for the dark field configuration, and the average of glass and water (~ 1.4) for the gold luminescence configuration.

Discussion

From the figure, it is first noted that both panels show a roughly linear relation between wavelength and antenna length. Furthermore, the luminescence wavelengths are red-shifted compared to the scattering wavelengths. This is the case for the measured data points and for the calculated values. Finally, it is noted that the dark field peaks lay in the center of the calculated band, whereas the luminescence peaks touch the top of the band.

It can be concluded that the resonance wavelengths for both data sets follow the trend predicted by theory. The red-shift for the luminescence peaks occurs because the antennas were covered with water, which has a higher refractive index than air.

Let us now discuss the fact that the dark field peaks fall in the center of the calculated band, while the luminescence peaks do not. At first, one might argue that the two measurements were done using different samples (Sample 1 and Sample 2, respectively), which could have different geometries. However, this explanation is unlikely, since the scanning electron microscope images presented in Section 5.1 do not show significant differences. We provide two alternative explanations: (1) While the dark field spectra were corrected for the sys-

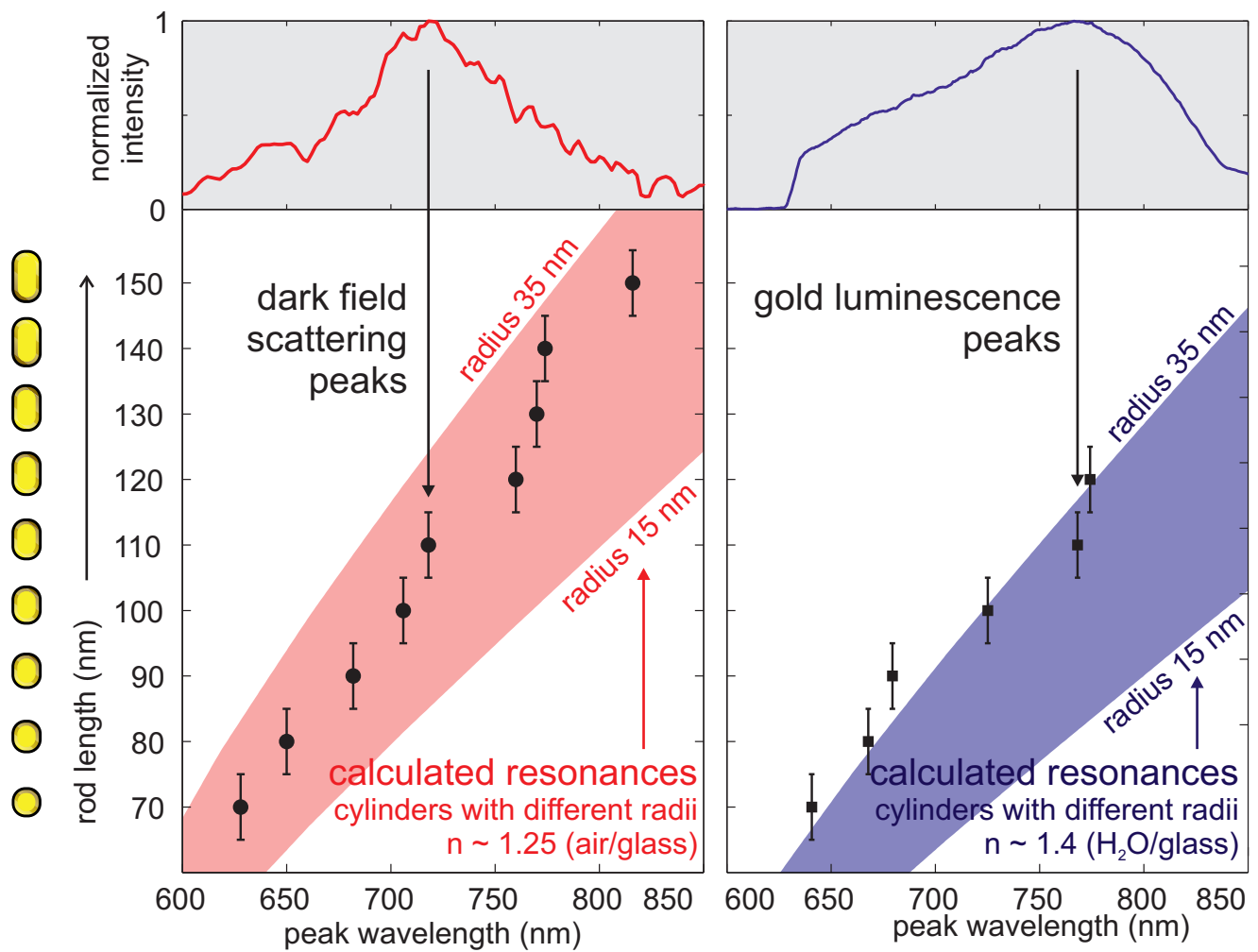


Figure 6.4: Measured dark field scattering peaks in air (*left*) and gold luminescence peaks in water (*right*) compared to theory.

tem's response function, the luminescence peaks were not. This is expected to distort the shape of the spectra. (2) The use of an average refractive index in the calculation may be inaccurate.

6.4 Lucigenin fluorescence and chemiluminescence

This section presents experimental results and a discussion on the chemiluminescence of lucigenin near the antennas. Lucigenin is not only a chemiluminescent reagent, but also a fluorophore. For this reason, the chemiluminescent system in this thesis has two emitting components: 1) N-methyl acridone, and 2) the lucigenin itself, excited by N-methyl acridone through Förster resonance energy transfer. The emission of the second component was studied first, using a blue LED to excite the lucigenin. A CCD image of the antenna area is shown in Fig. 6.5a. The image has the form of a circular spot. The bright irregular hexagon is the area where the gold flake for focused ion beam milling was located. The dark circle and the dark strips near the hexagon's right edge are remaining strips of gold. A close-up of the antenna array is shown in Fig. 6.5b. The nine circular spots correspond to the antenna locations. These spots are dark (less than 5000 counts in 15s) compared to the surrounding area (~5400 counts in 15 s).

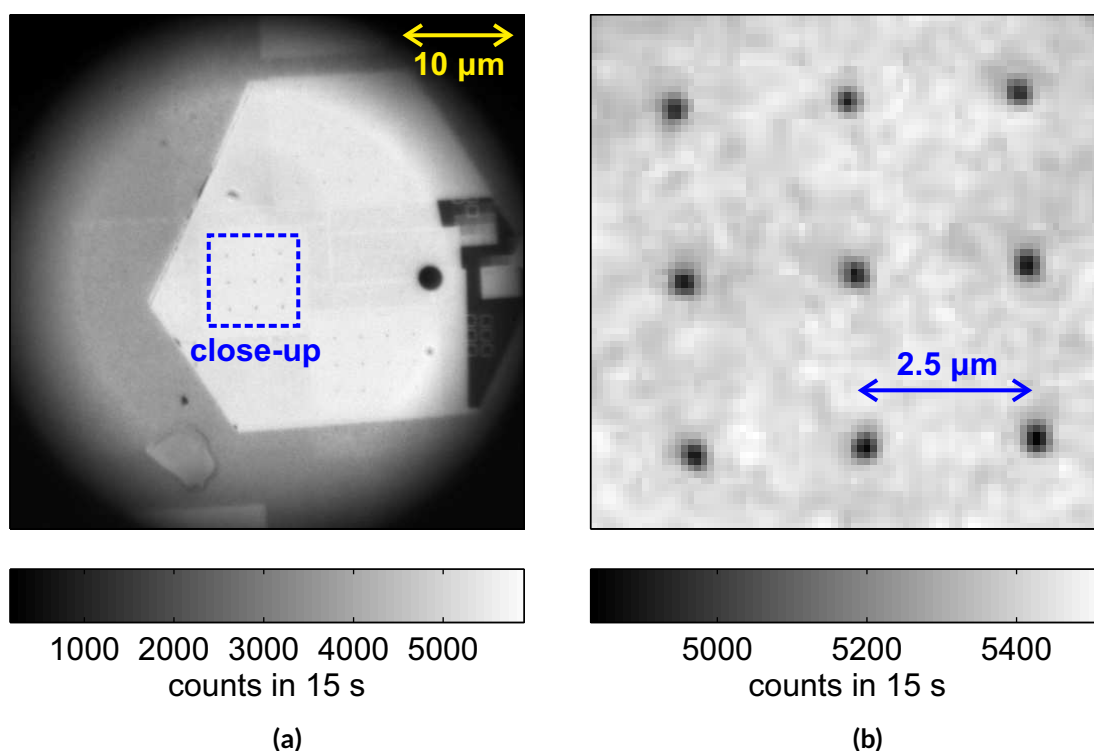


Figure 6.5: CCD images of lucigenin fluorescence near the antenna sample. (a) Overview of the antenna area. (b) Close-up of the nine antennas.

It was tested whether local excitation by a laser also leads to dark spots. The resulting SPAD scan (Fig. 6.6) shows that the antennas are again dark (less than 4000 counts) compared to the background (4100 - 4400 counts). It is noted that the background is non-uniform. The background is less intense at the top of the image (~4100 counts).

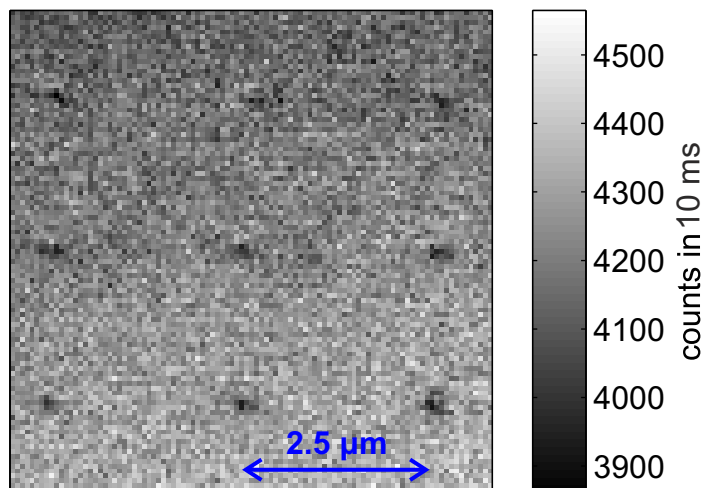


Figure 6.6: SPAD scan showing lucigenin fluorescence near the antenna sample, using a laser to excite the fluorophore locally.

Having studied the lucigenin component, the complete chemiluminescence system was studied next. This did not require excitation by light. The CCD image of the sample area is shown in Fig. 6.7a. We note that compared to Fig. 6.5a, the circular spot is displaced due to a slight misalignment of the CCD chip. Also, the background is non-uniform: the top of the image shows ~ 300 counts in 200 s, whereas the bottom of the image shows ~ 200 counts.

The close-up of the antennas (Fig. 6.7b) shows that the antennas darken again. Compared to Fig. 6.5b, there is less contrast with the background. Also, the dark spots have different intensities. Finally, as in the overview image, the background intensity is not uniform: the top of the scan has a higher intensity (~ 350 counts) than the bottom of the scan (~ 375 counts). The antenna intensities were not compared in a quantitative way, because the non-uniform background hinders a fair comparison.

Discussion

The observed darkening can be caused in several different ways. First of all the suboptimal overlap of the fluorescence spectrum with the resonances of the antennas can lead to a decrease in luminescence quantum yield. Also the relatively high intrinsic quantum yields of N-methyl acridone and lucigenin (~ 0.8 and ~ 0.4) can lead to a decrease in quantum yield, as was explained using the model of Section 4.2. Moreover, no matter what the intrinsic quantum yield is, close to the antenna the yield is strongly attenuated.

A second effect could be due to the large volume of emitters that is present in this experiment. For every fluorophore that is located close to the antenna in a region with enhancement there is a multitude of emitters that is far away from the antenna. All light emitted

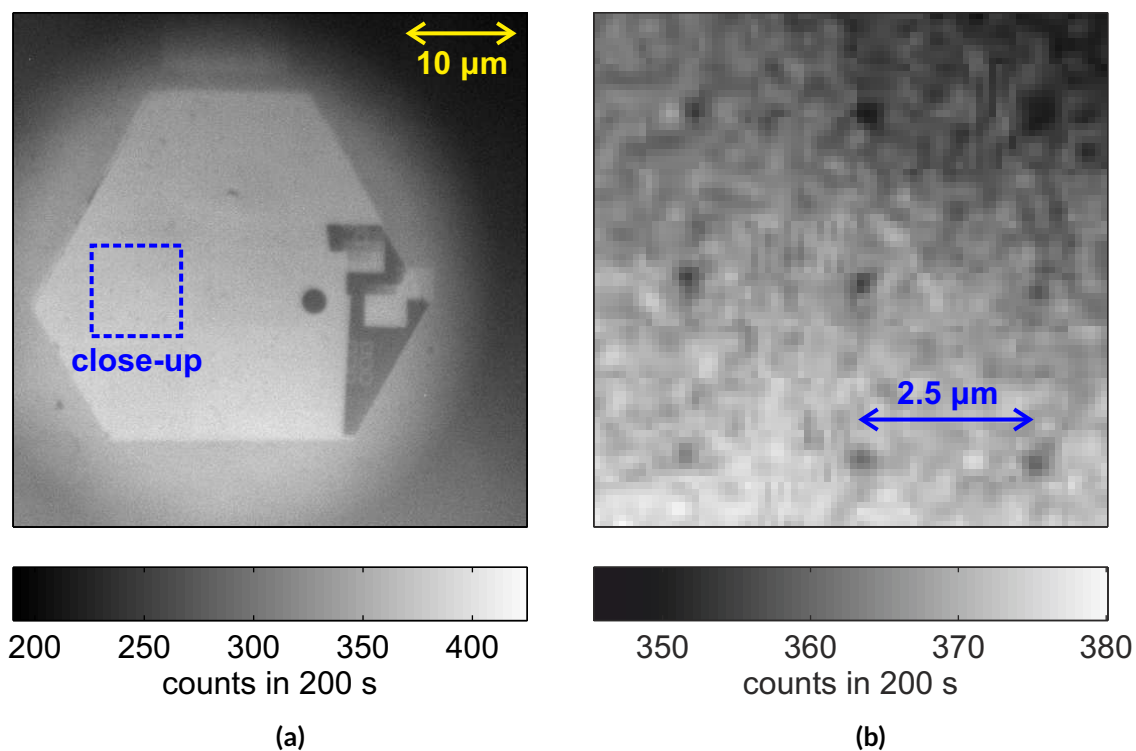


Figure 6.7: CCD images of lucigenin chemiluminescence near the antenna sample. (a) Overview of the antenna area. (b) Close-up of the nine antennas. A moving average was taken over a 3x3 pixel area to smooth the image.

by these molecules can lead to an enhanced signal if its light is scattered by the antenna to the detector. It can however also be that the light is absorbed by the antenna, leading to a decreased signal.

The non-uniform background for the chemiluminescence system can also have different causes. For one, the chemiluminescence reagents may not mix properly. In the present experiment, a hydrogen peroxide droplet falls onto a lucigenin droplet that is covering the sample. If the mixing is slow or chaotic, the density of emitters can vary throughout the volume of the liquid. This can lead to different areas of the sample being illuminated with different intensities. Such an effect can also arise when the luminescent droplet has an irregular shape or when the antennas are not perfectly in the center of the droplet.

6.5 Methylene blue fluorescence

6.5.1 Measured time traces

To aid the discussion on the darkened chemiluminescence, the performance of these structures was tested in a more controlled study, by monitoring fluorescence time-traces of methylene blue diffusing through an antenna's near-field. Methylene blue was used as the fluorophore because of its low quantum yield (1-2%) and better spectral overlap with the antenna resonances (see Fig. 6.2). A low concentration was used, so that only a few molecules are present in the illumination spot. The methylene blue fluorescence was monitored in time for 8 minutes near each antenna. A similar study has been performed by [8].

To illustrate the potential of time monitoring, the time trace for the 100 nm antenna is shown in Fig. 6.8 (red curve). There is a background signal of ~ 190 counts in 10 ms. Occasionally, there are sharp peaks, which we will refer to as fluorescence bursts. The highest burst occurs after ~ 6 minutes and shows 532 counts in 10 ms. A reference signal (blue curve), measured for the same antenna using water instead of methylene blue, does not show bursts. It should be noted that the red curve was measured with a polarization filter along the long axis of the antenna. For the blue curve, there was no polarization filter, resulting in a measured intensity that was roughly twice as high. To compare the two curves, the blue curve has been divided by two.

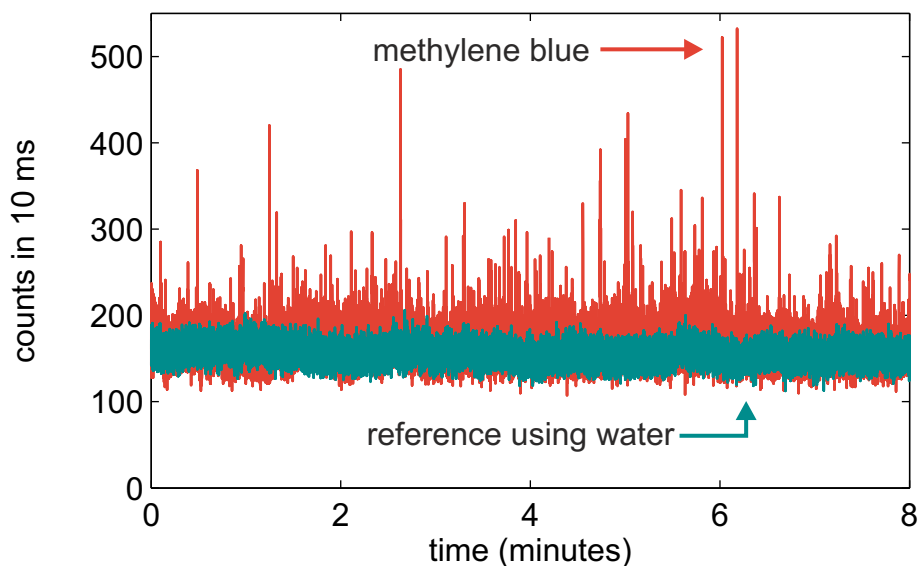


Figure 6.8: Measured fluorescence time trace near the 100 nm antenna for methylene blue (red curve), showing bursts. A reference signal (blue curve), measured for the same antenna in water instead of methylene blue, does not show bursts. As explained in the text, the reference curve has been divided by two.

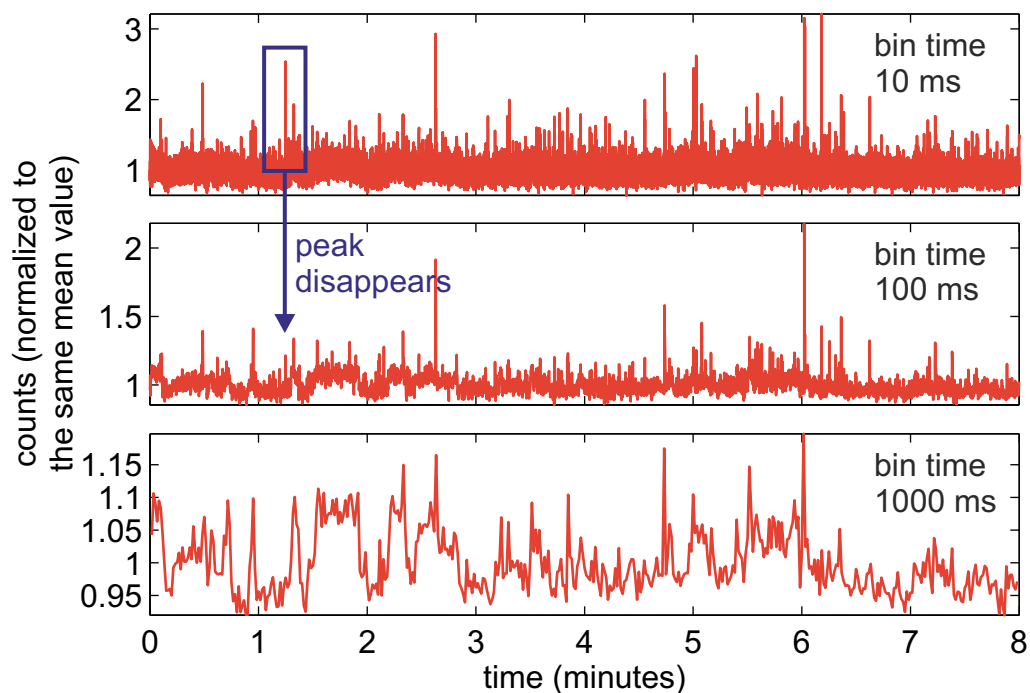


Figure 6.9: Fluorescence time trace for the 100 nm antenna, using different bin times. *Top:* 10 ms. *Middle:* 100 ms. *Bottom:* 1000 ms. The curves are normalized in such a way that they have the same mean value. When using higher bin times, the intensity fluctuations disappear.

It should be noted that bursts only show up when the time resolution is high enough. To demonstrate this, Fig. 6.9 shows the same time trace with different bin times. The trace with the lowest bin time (10 ms) shows most bursts. When using a higher bin time (100 ms), some of these bursts disappear. For example, the peak marked by the rectangle disappears. For the highest bin time (1000 ms), the intensity fluctuates, but there are no significant bursts.

Discussion

The background of the time trace in Fig. 6.8 is caused by 1) the gold luminescence, and 2) all fluorophores present in the illumination spot. The reference trace measured for the antenna in water shows only the luminescence. Comparing the two traces, it is noted that the fluorescence component is relatively small: ~ 20 counts in 10 ms. It is unclear how many fluorophores are present in the spot, because the concentration was unknown. With the concentration, one could calculate interesting physical parameters, e.g. the average number of molecules in the illumination spot, the molecular brightness (the average number of photons produced per molecule per unit time), and the antenna's enhancement factor [8].

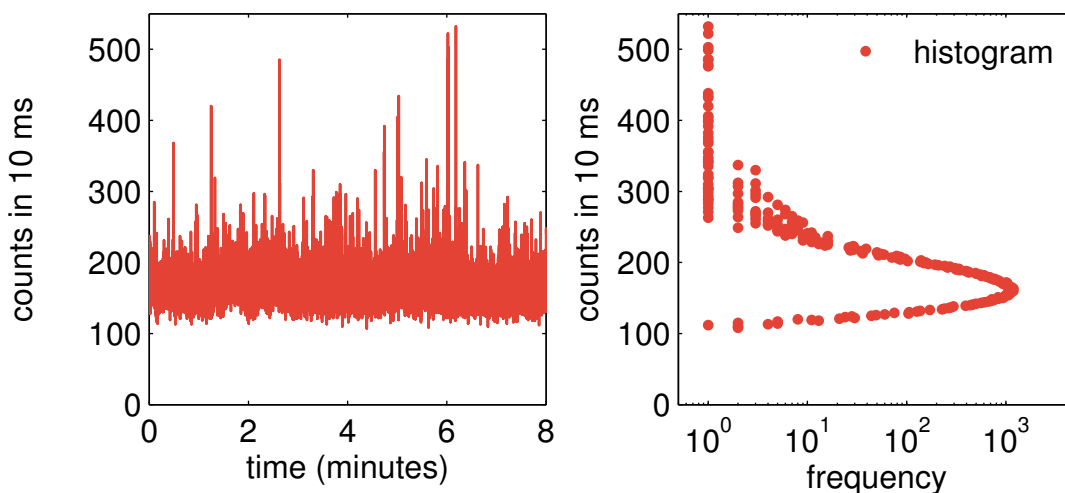


Figure 6.10: Fluorescence time trace for the 100 nm antenna (*left*), and photon count histogram constructed from this measurement (*right*).

6.5.2 Analysis using photon count histograms

As a tool to analyze the fluorescence bursts, we propose to use a photon count histogram (PCH). Such a histogram shows the frequency with which a certain number of counts is observed. The construction of a histogram is illustrated in Fig. 6.10. As the figure shows, the bursts in the time trace come back in the histogram as an asymmetric tail. The highest peak (532 counts) is located at the end of the tail. The histogram for the 100 nm antenna is shown again in Fig. 6.11a together with a Poissonian distribution based on the observed mean number of counts. Fig. 6.11b shows the PCH and Poissonian corresponding to an empty area, *i.e.* without antenna. It is noted that for the 100 nm antenna, the distribution strongly deviates from Poissonian statistics. There are numerous occurrences of high counts that would be highly unlikely in a Poisson distribution. For the empty area, however, the PCH is close to the Poissonian.

Discussion

To explain the deviation from Poissonian statistics, let us briefly discuss the PCHs used in standard fluorescence correlation spectroscopy (FCS) experiments [30]. For low-concentration fluorophores diffusing through a laser spot, the PCH is a super-Poissonian distribution. The broadening compared to a Poissonian is caused by (1) fluorescence intensity fluctuations due to the spatially varying excitation intensity of the laser beam, and (2) the fluctuation of the number of particles inside the excitation volume. For high fluorophore concentrations, both fluctuation sources become negligible, and the distribution approaches a Poissonian.

The fact that the empty area (Fig. 6.11b) shows a Poissonian distribution implies that the

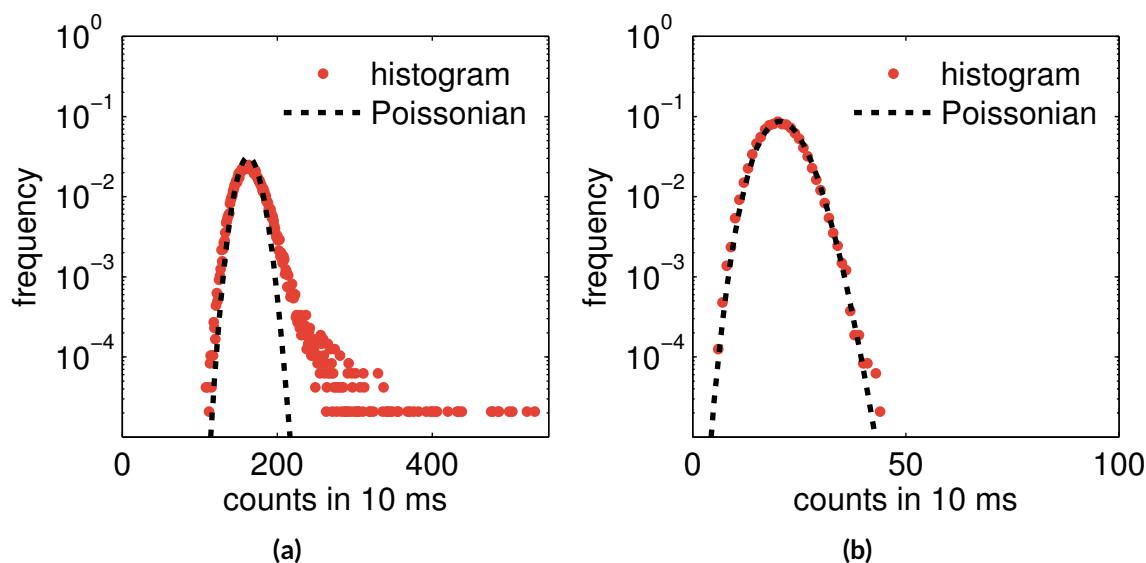


Figure 6.11: Photon count histograms for (a) the 100 nm antenna and (b) an area without antenna. The dotted line shows an expected Poissonian distribution based on the observed mean number of counts. For the 100 nm antenna, the distribution strongly deviates from Poissonian statistics.

fluorophore concentration is high enough to suppress the intensity fluctuations mentioned above. The deviation from Poissonian statistics for the 100 nm antenna (Fig. 6.11a) is explained as follows. Near an antenna, there is an additional source of intensity fluctuations, because the quantum yield of the fluorophore depends on the location with respect to the antenna.

6.5.3 Comparison of different-sized antennas

Let us now compare the PCHs of different-sized antennas. Fig. 6.12 shows the PCHs for the 70-120 nm antennas¹. As the figure shows, the distributions of the 100 and 110 nm antennas have the longest asymmetric tails. To make the analysis more quantitative, for each antenna the highest number of counts that occurred in 8 minutes is shown in Table 6.1. The difference between the mean number of counts and the modal (most frequent) number of counts is also shown. The 110 nm antenna has the largest difference between the mean and the mode (4.8%).

Discussion

Looking at the table, of all antennas, the 100 nm produced the strongest burst (532 counts). However, it cannot be concluded that the 100 nm antenna is best at enhancing methylene blue. It is possible that other antennas show higher bursts when monitoring for a sufficiently long time. The table also shows that the 110 nm antenna has the largest difference between

¹Data from the 130-150 nm antennas was also recorded, but is considered to be unreliable, because the setup's response function is low for high wavelengths. See Section 5.3.

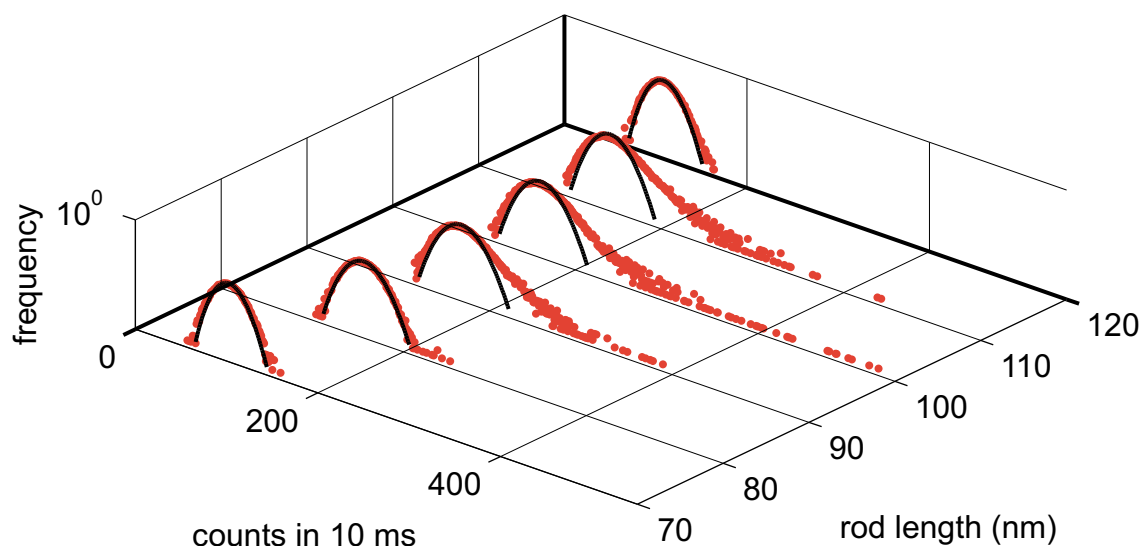


Figure 6.12: Photon count histograms for methylene blue near different-sized antennas.

antenna length (nm)	70	80	90	100	110	120
highest no. of counts	159	251	390	532	441	164
mean no. of counts	103.0	156.7	172.1	165.6	149.0	109.1
modal no. of counts	101	154	169	163	142	109
mean - mode (% difference)	+2.0%	+1.8%	+1.8%	+1.6 %	+4.8%	+0.1%

Table 6.1: Calculated difference between the mean and modal number of counts for each antenna.

mean and the mode (4.8%). From this percentage, one can conclude that in *comparison* to the other antennas, this antenna shows more enhancement. It should however be noted that the percentage is not the enhancement factor of the antenna. To explain this, let us consider a situation with a fluorophore in a very high concentration. In that case, while the antenna's enhancement factor is still the same, the PCH will approach a Poissonian, with no difference between the mean and the mode².

6.5.4 Control experiment using water

As a control experiment, time traces were also measured for the antennas in water. In principle, these signals only have the gold luminescence component, although occasionally fluorescence from a water contaminant may show up. Fig. 6.13 shows the PCHs for water. For the 80-110 nm antennas, the center of the methylene blue PCH shows more counts than the center of the water PCH. For the 70 and 120 nm antenna, however, the PCH of the methylene blue shows *less* counts than the water PCH.

²Strictly speaking, there could be a difference of maximum 1 count, because the mode is always an integer, while the mean can be a decimal number.

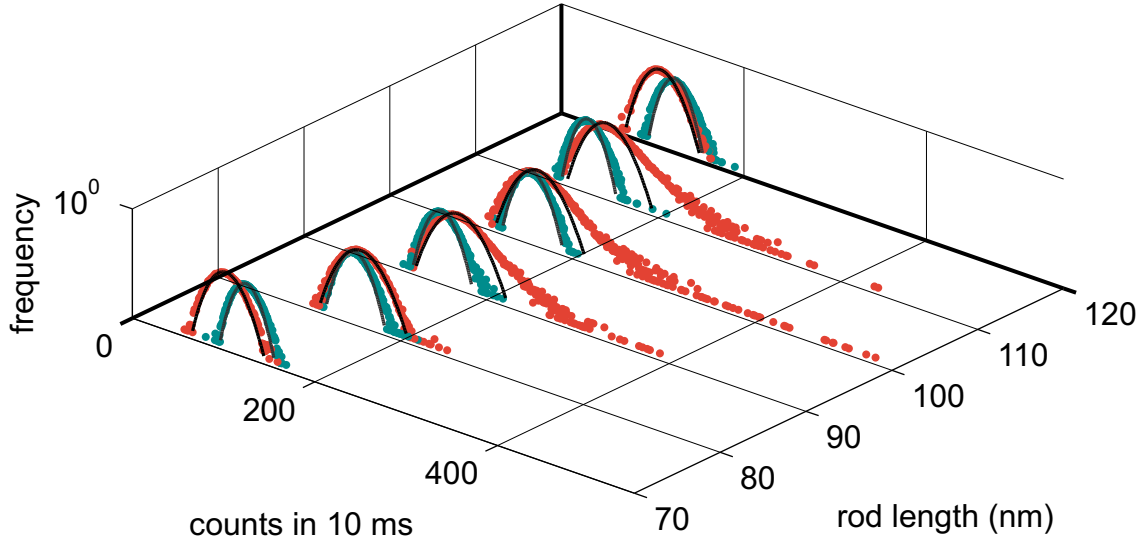


Figure 6.13: Photon count histograms for methylene blue (shown in red) and water (shown in blue) near different-sized antennas.

antenna length (nm)	70	80	90	100	110	120
enhancement factor	-3.5	1.1	3.2	1.6	3.9	-2.5

Table 6.2: Calculated enhancement factor for each antenna. The calculation was done using Eq. 6.1.

Using the control experiment, it is possible to obtain the enhancement factor for each antenna. The calculation is based on the total number of counts in each time trace. For a methylene blue time trace, we denote the total number of counts in 8 minutes as M_i , with i an index of the antenna ($i = 1$ corresponding to the shortest antenna). For a water time trace, the total is denoted by W_i . The time traces corresponding to an area *without* antenna are denoted by $M_{no\ antenna}$ and $W_{no\ antenna}$. For a single antenna with index i , the enhancement factor is given by

$$f_i = \frac{M_i - W_i}{M_{no\ antenna} - W_{no\ antenna}} \quad (6.1)$$

Here, W_i is subtracted to remove the gold luminescence component, so that only the signal of the fluorescence remains. This signal is then compared to the fluorescence in an area without an antenna ($M_{no\ antenna} - W_{no\ antenna}$). Table 6.2 shows the calculated enhancement factor for each antenna.

Discussion

Methylene blue is expected to show more counts than water because for methylene blue there is not only the gold luminescence component, but also a fluorescence component. The reason that for the 70 and 120 nm, less counts are observed, can be explained in several ways. There may have been an experimental error, e.g. a misalignment of the laser's focal

spot. However, this is unlikely because before measuring each time trace, the position of the laser spot was optimized by maximizing the gold luminescence signal. Besides, a repeated measurement for the 110 nm rod led to the same result. To find out whether this is an experimental error or a physical effect, additional measurements are required.

From the enhancement factors in Table 6.2, it is concluded that the 110 nm rod performs best, with an enhancement factor of ~ 4 . The 70 and 120 nm have negative enhancement factors because, as discussed above, these rods show a lower signal in methylene blue than in water. The reader is reminded that the spectral overlap between the methylene blue emission and the antenna resonances was highest for the 80 and 90 nm rods (see Fig. 6.3). The antenna showing the best enhancement is thus 20-30 nm longer than the antennas with the best spectral overlap. There are studies reporting a red-shift between the enhancement peak and the plasmon resonance [27]. This red-shift has been briefly discussed in Section 4.2. However, to reach a stronger conclusion on this wavelength shift, further investigation is required.

7 Conclusion and outlook

We have studied intensity enhancement of chemiluminescence and fluorescence near optical antennas. We control the plasmon resonance wavelengths of the antennas by varying the length. The plasmon resonances were characterized using 1) dark-field scattering spectroscopy and 2) spectroscopy of the intrinsic luminescence of the antenna material (gold). We observe an approximately linear relation between the resonance wavelength and antenna length, which is in good agreement with a Fabry-Perot resonator model for cylindrical antennas [2].

We have presented experiments in which the antennas are covered by a chemiluminescent droplet containing lucigenin. We observe a decreased intensity near the antennas, and provide two main explanations: 1) Emitters *close* to the antenna experience a decreased radiative decay rate. 2) Light from emitters *far* from the antenna is absorbed or scattered away from the detector. In the latter case, emitters *close* to the antenna may still show an increased radiative decay rate.

To eliminate the influence of emitters far from the antenna, we suggest three improvements to the experimental procedure. First of all, the reaction can be forced to occur in close proximity to the antennas by covering the sample with a spin-coated layer that contains one of the chemiluminescence reagents. Secondly, one can selectively collect light emitted close to the glass surface, by detecting angles corresponding to total internal reflection. Finally, one can design an antenna with a directional emission pattern and collect this directed emission.

We note that there are three strict conditions that must be met for enhancement to occur. 1) The emitter should have a low intrinsic quantum yield. 2) The emission should spectrally overlap with the antenna resonances. 3) The emitter should have a favorable location with respect to the antenna.

The observed chemiluminescence images show non-uniform intensities. We suspect that the emitters are not evenly distributed within the droplet due to slow or improper mixing of the reagents. Thus, if a chemiluminescence system shows bad mixing, emitters may be created at locations that are highly *unfavorable*, where there is no interaction with the antenna.

We expect that a metal nanostructure can in principle enhance chemiluminescence via plasmons, but that the system needs careful design to make sure that emitters are created close to the structure, where enhancement can occur. This could be realized using an integrated nanofluidic device in which the reagents mix when they are close to the plasmonic structure.

Finally, we presented a controlled study on distance dependent enhancement, using a flu-

orophore with a low intrinsic quantum yield and better spectral overlap with the antennas (methylene blue). In particular, by using a low-concentration, we ensure that occasionally an excited emitter diffuses through a favorable spot where the enhancement is high. When monitoring the fluorescence intensity in time, we observe sharp, narrow peaks, which we refer to as fluorescence bursts. We claim that these bursts occur whenever an emitter is in a favorable location. Comparing the different-sized antennas, we conclude that a 70x110 nm antenna causes a ~4x enhancement of the fluorescence intensity.

We pioneered the use of photon count histograms as a tool to analyze the fluorescence bursts. Such histograms show strong deviations from Poissonian statistics in the form of large asymmetric tails. We claim that the deviation from Poissonian statistics is caused by fluctuations in the fluorescence intensity. These intensity fluctuations arise as the molecules diffuse randomly through the spatially varying enhancement profile around the antenna. The observed photon count histograms form a strong signature of enhanced emission near an optical antenna. We anticipate that this method could be generalized to provide subdiffraction-limited information on spatially-varying enhancement near a nanostructure.

References

- [1] K. Aslan and C.D. Geddes. Metal-enhanced chemiluminescence: advanced chemiluminescence concepts for the 21st century. *Chem. Soc. Rev.*, 38:2556–2564, 2009.
- [2] L. Novotny. Effective wavelength scaling for optical antennas. *Physical Review Letters*, 98(26):266802, June 2007.
- [3] A. Roda, P. Pasini, M. Guardigli, M. Baraldini, M. Musiani, and M. Mirasoli. Bio- and chemiluminescence in bioanalysis. *Fresenius' Journal of Analytical Chemistry*, 366(6-7):752–759, 2000.
- [4] L.J. Kricka. Clinical applications of chemiluminescence. *Analytica Chimica Acta*, 500(1-2):279 – 286, 2003.
- [5] F. Barni, S.W. Lewis, A. Berti, G.M. Miskelly, and G. Lago. Forensic application of the luminol reaction as a presumptive test for latent blood detection. *Talanta*, 72(3):896 – 913, 2007.
- [6] C. Dodeigne, L. Thunus, and R. Lejeune. Chemiluminescence as diagnostic tool. a review. *Talanta*, 51(3):415 – 439, 2000.
- [7] W.L. Vos, A.F. Koenderink, and I.S. Nikolaev. Orientation-dependent spontaneous emission rates of a two-level quantum emitter in any nanophotonic environment. *Phys. Rev. A*, 80:053802, 2009.
- [8] H. Yuan, S. Khatua, P. Zijlstra, M. Yorulmaz, and M. Orrit. Thousand-fold enhancement of single-molecule fluorescence near a single gold nanorod. *Angewandte Chemie International Edition*, 52(4):1217–1221, 2013.
- [9] A. Kinkhabwala, Z. Yu, S. Fan, Y. Avlasevich, K. Müllen, and W.E. Moerner. Large single-molecule fluorescence enhancements produced by a bowtie nanoantenna. *Nature Photonics*, 3(11):654–657, 2009.
- [10] M.H. Chowdhury, K. Aslan, S.N. Malyn, J.R. Lakowicz, and C.D. Geddes. Metal-enhanced chemiluminescence: Radiating plasmons generated from chemically induced electronic excited states. *Applied physics letters*, 88(17):173104–173104, 2006.
- [11] M.H. Chowdhury, K. Aslan, S.N. Malyn, J.R. Lakowicz, and C.D. Geddes. First observation of surface plasmon-coupled chemiluminescence (spcc). *Chemical physics letters*, 435(1):114–118, 2007.
- [12] M. Fox. *Quantum Optics: An Introduction*. Oxford University Press, 2006.

- [13] J.R. Lakowicz. *Principles of fluorescence spectroscopy*. Springer, 2009.
- [14] D.A. McQuarrie and J.D. Simon. *Physical Chemistry: A Molecular Approach*. University Science Books, 1997.
- [15] Z-F. Zhang, H. Cui, C.-Z. Lai, and L.-J. Liu. Gold nanoparticle-catalyzed luminol chemiluminescence and its analytical applications. *Analytical chemistry*, 77(10):3324–3329, 2005.
- [16] K.D. Gundermann and F. McCapra. *Chemiluminescence in Organic Chemistry*. Reactivity and Structure: Concepts in Organic Chemistry. Springer London, Limited, 2011.
- [17] L. Novotny and N. van Hulst. Antennas for light. *Nature Photonics*, 5:83–90, 2011.
- [18] L. Novotny and B. Hecht. *Principles of Nano-Optics*. Cambridge University Press, 2nd edition, 2012.
- [19] D. Attwood. *Soft X-Rays and Extreme Ultraviolet Radiation: Principles and Applications*, chapter 6. Cambridge University Press, 1999.
- [20] P. B. Johnson and R. W. Christy. Optical constants of the noble metals. *Phys. Rev. B*, 6:4370–4379, Dec 1972.
- [21] P. Bharadwaj, B. Deutsch, and L. Novotny. Optical antennas. *Adv. Opt. Photon.*, 1(3):438–483, 2009.
- [22] J.A. Schuller, E.S. Barnard, W. Cai, Y.C. Jun, J.S. White, and M.L. Brongersma. Plasmonics for extreme light concentration and manipulation. *Nature Materials*, 9(3):193–204, March 2010.
- [23] S.A. Maier. Localized surface plasmons. In *Plasmonics: Fundamentals and Applications*, pages 65–88. Springer US, 2007.
- [24] D.J. Griffiths. *Introduction to electrodynamics*. Prentice Hall, Upper Saddle River, N.J., 1999.
- [25] P. Biagioni, J-S. Huang, and Bert Hecht. Nanoantennas for visible and infrared radiation. *Reports on Progress in Physics*, 75(2):024402, 2012.
- [26] L. Novotny and C. Hafner. Light propagation in a cylindrical waveguide with a complex, metallic, dielectric function. *Physical review E*, 50(5):4094, 1994.
- [27] P. Bharadwaj and L. Novotny. Spectral dependence of single molecule fluorescence enhancement. *Optics Express*, 15:14266, 2007.
- [28] J. Prangsma, P. Biagioni, and B. Hecht. *Fabrication and optical characterization of nanoantennas*, chapter 13, pages 215–233. Cambridge University Press, 2013.

- [29] L. Meijer. Ldos modification for fluorescence quantum efficiency measurements. Master's thesis, University of Twente, 2013.
- [30] Y. Chen, J.D Müller, P.T.C. So, and E. Gratton. The photon counting histogram in fluorescence fluctuation spectroscopy. *Biophysical journal*, 77(1):553–567, 1999.

A Details of the experiments with the fluorescence microscope

- **Gold luminescence spectra.** The antennas were covered with $200\mu\text{L}$ water. The excitation was centered at 620 nm and cleaned up by a 532 long-pass and 633 short-pass filter. Besides, the excitation was polarized along the *short* axis of the rods. In the detection pathway, a 633 long-pass filter was used. A polarizer was present in the detection pathway, transmitting the "long mode" off the antenna.
- **Imaging lucigenin fluorescence with lamp.** The antennas were covered with a droplet of lucigenin. No laser excitation was used. Instead, the droplet was fully illuminated by a blue LED. The emitted light was filtered by a 532 long-pass filter and guided to the EMCCD camera. No polarizer was present in the detection pathway. The lucigenin was obtained from Sigma-Aldrich.
- **Imaging lucigenin fluorescence with a laser.** The excitation was centered at 515 nm and cleaned up by 515/10 band-pass filter. The emitted light was filtered by a 532 long-pass filter and guided to the SPAD. An image was obtained by performing a two-dimensional scan with the piezo stage. No polarizer was present in the detection pathway. The lucigenin was obtained from Sigma-Aldrich.
- **Imaging lucigenin chemiluminescence.** Before the reaction, a droplet of lucigenin solution was present on the antenna substrate. To trigger the reaction, a droplet of hydrogen peroxide was added. The emitted light was filtered by a 532 long-pass filter and guided to the EMCCD camera. No polarizer was present in the detection pathway. The lucigenin, hydrogen peroxide and sodium hydroxide were obtained from Sigma-Aldrich.
- **Monitoring methylene blue fluorescence.** A methylene blue stock solution of unknown concentration, kindly provided by Dr. R. Gill, was filtered ¹ and diluted 10^3x using water. The excitation was centered at 620 nm and cleaned up by a 532 long-pass and 633 short-pass filter. A polarizer was present in the detection pathway, transmitting the "long mode" off the antenna.
- **Control experiment using water.** The antennas were covered with $200\mu\text{L}$ water. The excitation was centered at 620 nm and cleaned up by a 532 long-pass and 633 short-pass filter. Besides, the excitation was polarized along the *short* axis of the rods. In

¹During preliminary experiments, fluorescent agglomerates were observed.

the detection pathway, a 633 long-pass filter was used. A polarizer was present in the detection pathway, transmitting the "long mode" off the antenna. No polarizer was present in the detection pathway.